

# LPI Summer Intern Program in Planetary Science

PAPERS PRESENTED AT THE

**38<sup>TH</sup> SUMMER INTERN  
CONFERENCE**

**AUGUST 9, 2023  
HOUSTON, TX**





*Papers Presented at the*

# **Thirty-Eighth Annual Summer Intern Conference**

**August 9, 2023**

2023 Summer Intern Program for Undergraduates  
Lunar and Planetary Institute

Sponsored by  
Lunar and Planetary Institute  
NASA Johnson Space Center



Compiled in 2023 by

Meeting and Publication Services  
Lunar and Planetary Institute  
USRA Houston  
3600 Bay Area Boulevard, Houston TX 77058-1113

The Lunar and Planetary Institute is operated by the Universities Space Research Association under a cooperative agreement with the Science Mission Directorate of the National Aeronautics and Space Administration.

Any opinions, findings, and conclusions or recommendations expressed in this volume are those of the author(s) and do not necessarily reflect the views of the National Aeronautics and Space Administration.

Material in this volume may be copied without restraint for library, abstract service, education, or personal research purposes; however, republication of any paper or portion thereof requires the written permission of the authors as well as the appropriate acknowledgment of this publication.

## HIGHLIGHTS

---

### LPI Summer Intern Program 2023 — Planetary Science Seminars

*Facilitated by Julie Stopar and Claudia Bellard*

Date	Speaker	Topic
June 7	Prajakta Mane	Meteorites and the Early Solar System
June 14	Kennda Lynch	Astrobiology Primer
June 21	Patrick McGovern	Tectonics of Icy Worlds: Examples from Pluto and Several Giant Planet Moons
June 28	Juliane Gross	Lunar Samples and Preparing for Artemis
July 5	Walter Kiefer	Evolution of Venus: Modeling & Spacecraft Missions
July 12	Interns	Mid-Term Presentations
July 19	Liz Rampe	Mars Missions
July 26	Tabb Prissel	Planetary Petrology

### LPI Summer Intern Program 2023 — Professional Development Seminars

*Facilitated by Christine Shupla, Julie Stopar, and Grace Beaudoin*

Date	Speaker	Topic
June 8	Presenter: Julie Stopar  Panelists: Walter Kiefer, Scott Eckley, Germán Martínez, and Laura Rodriguez	<b>The Business of Planetary Science</b> Learn about how Planetary Science gets done and what career paths are available in the field.
June 16	Presenters: Julie Stopar and Allan Treiman  Panelists: Germán Martínez, Cyrena Goodrich, and Allan Treiman	<b>A How to Guide to Scientific Writing</b> 1) In preparation for your final project reports, you'll be guided through best practices for writing a scientific abstract. 2) Work with a planetary scientist to prepare a draft Planetary News article the week before and bring it to the seminar to get feedback.
July 7	Presenter: Julie Stopar  Panelists: Gabriel Eggers, Thomas Barrett, Prajkta Mane	<b>Presenting Your Research</b> In preparation for the midterm reports, you'll be guided through best practices for presenting your research.
July 13	Presenter: Kennda Lynch  Panelists: Aditi Pandey, Brendan Anzures and Paul Schenk	<b>Diversity and Inclusion in Planetary Science</b> A diverse and equitable community can reach for the stars! Learn about the state of our profession and its future.
July 21	Panelists: Brian Balta, Paul Schenk, and Laura Rodriguez	<b>Pursuing Graduate Studies in Planetary Science</b> To prepare you for the application process, our panel will give you advice on how to apply and succeed in graduate school.

## HIGHLIGHTS

---

### LPI Summer Intern Special Seminar

*Facilitated by LPI and NASA Johnson Space Center, Astromaterials Research and Exploration Science Division*

Date	Topic
July 6	LPI-ARES Science Symposium

### LPI Intern Stories Series

*Webinar facilitated by Grace Beaudoin*

Date	Stories	Topic
August 2	Elana Alevy, Claudia Bellard, Candice DeAnda, Danielle Kallenborn, Kyla Malo, and Jared McCallion	During LPI Intern Stories 2023, you'll hear from LPI Summer Interns about how they applied and prepared for their internship, their ongoing experiences, and how the internship has helped them.

### LPI Summer Intern Tours

*NASA Johnson Space Center*

Date	Speaker	Topic
June 29	Shaun Azimi	Robotics
July 6	Suzanne Foxworth and Kim Willis	Lunar Curatorial Laboratory
July 6	Mark Cintala	Experimental Impact Laboratory
July 6	Kevin Righter	Meteorite Laboratory
July 6	Everett Gibson	Apollo Tools and Core Tube
July 14	Angela Prince and Gail Schneider	Neutral Buoyancy Laboratory
July 27	Asher Lieberman	Video Wall – Lunar Rover VR – Lunar EVA Beta Dome – Orion Docking

## HIGHLIGHTS

---

### LPI Summer Intern Social Events

*Movie/games facilitated by Rachel Slank, Nicole Nevill, and Matthew Weller*

*National Intern Day facilitated by Claudia Bellard and Delia Enriquez*

<b>Date</b>	<b>Event</b>
June 7	LPI Scavenger Hunt
June 15	USRA/LPI Summer BBQ
June 20	Board Game Night
June 30	Cultural Sharing Night
July 14	Movie: Rocket Man
July 27	National Intern Day and Ice Cream
July 28	Murder Mystery
August 3	Movie: Evolution

### LPI Summer Intern Alumni Event

*Facilitated by Delia Enriquez and Julie Stopar*

<b>Date</b>	<b>Speaker</b>
August 10	David Melendrez Kelsey Prissel





## AGENDA

---

Wednesday, August 9, 2023

9:15 a.m.

Chairs: Julie Stopar and Prajka Mane

*Continental breakfast and coffee will begin at 8:30 a.m.*

Time	Speaker	Presentation Title
9:15 a.m.	Lisa Gaddis and Justin Filiberto	Welcoming Remarks
9:20 a.m.	KYLA MALO Carleton University Advisors: Kennda Lynch and Carina Lee	<i>Developing a Rapid 16s rRNA Sequencing Protocol for Bioremediation of Martian Regolith for Sustainable Agriculture</i> [#4008] To test the success of bioremediation efforts on martian regolith simulants, changes in the inoculated microbiome must be tested. As such, a rapid 16s rRNA sequencing protocol was specifically developed for sustainable agriculture.
9:32 a.m.	MADLINE WALTERS Tufts University Advisors: Tanya Peretyazhko, Silas Ralston, and Brad Sutter	<i>The Formation of Sulfate and Carbonate Evaporites in CO<sub>2</sub> Rich and CO<sub>2</sub> Poor Environments</i> [#4001] Studying the formation conditions of sulfate and carbonate evaporites on Mars results in Ca and Mg sulfates and amorphous calcium carbonate.
9:44 a.m.	CANDICE DE ANDA California State University Advisor: Liz Rampe	<i>Mineral Assemblages in Eskers from Iceland: An Analog for Cold and Wet Environments on Mars</i> [#4007] Esker samples collected from a Mars analog environment were studied using XRD to define mineralogical composition in order to determine if a mineralogical signature could be used to help identify the features on Mars.
9:56 a.m.	PRAGYA RAGHAV Zakir Hussain College of Engineering and Technology, Aligarh Muslim University Advisor: Germán Martínez	<i>Analysis of the Surface Albedo at Jezero Crater as Determined from the Meteorological Station On Board NASA's Mars 2020 Mission</i> [#4010] This study comprises analysis of albedo as a function of viewing geometry and illumination. The data was measured by the TIRS and RDS sensors present on the Mars Environmental Dynamics Analyzer (MEDA) meteorological station onboard NASA's Mars 2020 mission.
10:08 a.m.	JARED MCCALLION Rowan University Advisors: Samuel Lawrence and Julie Stopar	<i>Morphometric Characterization of Lunar Landing Sites</i> [#4013] In this project, we determine the physical parameters of the lunar surface at 16 successful lunar landing sites where LROC observations have been used to create digital terrain models.
10:20 a.m.	CHLOE LOCKE Colorado School of Mines Advisors: Thomas Barrett and John Gruener	<i>Standardizing a Method for Creating a Multilayered Regolith Simulant Testbed</i> [#4005] Experimentally standardizing a method to recreate density conditions on the lunar surface using lunar regolith simulants while making testbeds.

<b>Time</b>	<b>Speaker</b>	<b>Presentation Title</b>
10:32 a.m.	DANIELLE KALLENBORN Imperial College London Advisor: David Kring	<i>Rays of Schrödinger Impact Ejecta and Implications for Cratering Processes</i> [#4012] We identified and measured individual craters along the two main Schrödinger crater rays, Vallis Schrödinger and Vallis Planck. Based on these measurements we were able to constrain the processes of the primary impact event.
10:44 a.m.		<i>Break</i>
10:56 a.m.	AMELIA ASCIONE Rutgers University Advisors: Rachel Slank and Gabe Eggers	<i>Investigating Lunar Subsurface Cavities on the Moon Using Thermal Inertia and Temperature Maximum to Minimum Ratios</i> [#4006] We tested the capabilities of two techniques for detecting subsurface cavities on the Moon. Using thermal inertia and temperature maximum to minimum ratios, we successfully discovered a lava tube and other subsurface cavities.
11:08 a.m.	LEX SCHULTZ Yale University Advisor: Pat McGovern	<i>Topographic Characterization and Evolutionary Modeling of Large Volcano-Tectonic Structures on Venus</i> [#4002] What's in a name? That which we call a corona might be a volcano, but uneasy lies the edifice that wears the crown.
11:20 a.m.	ANDREW GMEREK SUNY University at Buffalo Advisors: Matt Weller and Walter Kiefer	<i>Mapping and Analysis of Ganis Chasma Rift System, Atla Regio, Venus</i> [#4009] Ganis Chasma is a complex rift with an interior unlike rifts seen anywhere else. It has remained tectonically poorly studied so we have generated a detailed fault map of Ganis to understand the history of rifting in this region.
11:32 a.m.	MIA RUDIN University of Texas at Dallas Advisor: Brian Balta	<i>Testing Hypotheses for the Origin of Martian Alkali Basalts Through Fractional Crystallization of Primary Magmas</i> [#4004] Context for the formation of the alkali basalts found at Gale Crater will benefit the understanding of Martian magmatism. We use the THERMOCALC algorithm MAGEMin to model the formation of these alkali basalts, suggesting a metasomatized source.
11:44 a.m.	TORI BURNETTE University of Texas at Austin Advisors: Prajka Mane and Timmons Erickson	<i>Stories of CAIs Revealed Through Secondary Processes</i> [#4003] A descriptive study of the mineralogy and textures of three calcium-aluminum inclusions (CAIs) from three separate chondritic meteorites focusing on the alterations they experienced and what those processes tell us about their time in the solar system.
11:56 a.m.	ELANA ALEVY Colby College Advisors: Nicole Nevill and Kaitlyn McCain	<i>Tracing Presolar Grain Populations: A New Matrix Chemistry Approach</i> [#4011] Using SEM-EDS and NanoSIMS, we attempt to measure micrometer-scale chemistry variations due to parent body processing within ALHA77307 to assess which matrix regions contain greater populations of presolar grains.
12:08 p.m.	Julie Stopar	<i>Wrap Up and Closing Remarks</i>
12:15 p.m.		<i>Adjourn (interns and advisors meet in Great Room for group photo)</i>

## CONTENTS

Tracing Presolar Grain Populations: A New Matrix Chemistry Approach <i>E. G. Alevy, N. D. Nevill, K. A. McCain, and A. N. Nguyen</i> .....	4011
Investigating Lunar Subsurface Cavities on the Moon Using Thermal Inertia and Temperature Maximum to Minimum Ratios <i>A. R. Ascione, R. A. Slank, and G. L. Eggers</i> .....	4006
Stories of CAIs Revealed Through Secondary Processes <i>V. E. Burnette, P. Mane, and T. Erickson</i> .....	4003
Mineral Assemblages in Eskers from Iceland: An Analog for Cold and Wet Environments on Mars <i>C. L. De Anda and E. B. Rampe</i> .....	4007
Mapping and Analysis of Ganis Chasma Rift System, Atla Regio, Venus <i>A. T. Gmerek, M. B. Weller, and W. S. Kiefer</i> .....	4009
Rays of Schrödinger Impact Ejecta and Implications for Cratering Processes <i>D. P. Kallenborn and D. A. Kring</i> .....	4012
Standardizing a Method for Creating a Multilayered Regolith Simulant Testbed <i>C. G. Locke, R. N. Kovtun, T. J. Barrett, and J. E. Gruener</i> .....	4005
Developing a Rapid 16s rRNA Sequencing Protocol for Bioremediation of Martian Regolith for Sustainable Agriculture <i>K. Malo, K. Lynch, J. Lopez, A. Simpson, and R. Loureiro</i> .....	4008
Morphometric Characterization of Lunar Landing Sites <i>J. M. McCallion, S. J. Lawrence, and J. D. Stopar</i> .....	4013
Analysis of the Surface Albedo at Jezero Crater as Determined from the Meteorological Station On Board NASA's Mars 2020 Mission <i>P. Raghav and G. M. Martínez</i> .....	4010
Testing Hypotheses for the Origin of Martian Alkali Basalts Through Fractional Crystallization of Primary Magmas <i>M. C. Rudin and J. B. Balta</i> .....	4004
Topographic Characterization and Evolutionary Modeling of Large Volcano-Tectonic Structures on Venus <i>A. K. Schultz and P. J. McGovern</i> .....	4002
The Formation of Sulfate and Carbonate Evaporites in CO <sub>2</sub> Rich and CO <sub>2</sub> Poor Environments <i>M. E. Walters, T. S. Peretyazhko, S. J. Ralston, B. Sutter, and P. D. Casbeer</i> .....	4001



**TRACING PRESOLAR GRAIN POPULATIONS: A NEW MATRIX CHEMISTRY APPROACH.** E. G. Alevy<sup>1,2,3</sup>, N. D. Nevill<sup>1,2,4</sup>, K. A. McCain<sup>5</sup>, and A. N. Nguyen<sup>2</sup> <sup>1</sup>Lunar and Planetary Institute, Universities Space Research Association, Houston, TX, 77058, <sup>2</sup>Astromaterials Research and Exploration Science, NASA Johnson Space Center, Houston, TX, 77058, <sup>3</sup>Department of Geology, Colby College, Waterville ME 04901, <sup>4</sup>Space Science and Technology Centre, School of Earth and Planetary Sciences, Curtin University, Perth, Western Australia, 6845, <sup>5</sup>Jacobs JETSII contract, NASA Johnson Space Center, Houston, TX 77058.

**Introduction:** Presolar grains are solidified remnants of stellar matter that can be identified through their extreme isotopic anomalies which exceed those found within solar environments. Found in primitive astromaterials, presolar grains preserve environmental signatures and records of physical and chemical processes occurring in the asymptotic giant branch (AGB) stars, nova, or supernova environments within which they formed. Therefore, analysis of presolar grains provides a direct snapshot of processes including nucleosynthesis, stellar dust formation, and galactic chemical evolution [1].

After incorporation into the solar system, presolar grains experienced aqueous and thermal processing of their meteorite parent bodies [2]. Aqueous alteration can not only destroy presolar grains (particularly presolar silicate phases) [3] but also re-equilibrate their isotopic compositions and alter their chemistries [4]. Here, we attempt to measure micrometer-scale chemistry variations due to parent body processing within the same meteorite to assess which matrix regions will have greater populations of presolar grains.

Nanoscale Secondary Ion Mass Spectrometry (NanoSIMS) is currently used for rapid, *in situ* presolar grain identification. However, NanoSIMS analysis is partially destructive and requires multiple weeks of data collection to assess multiple matrix areas in a meteorite. To identify presolar grain populations while best preserving analysis time and astromaterials, we test a new method to characterize micrometer-scale changes in matrix alteration based on a qualitative, Scanning Electron Microscope (SEM)-based analysis of five matrix regions in ALHA77307, a CO3.0 chondrite. Subsequently, we searched for presolar grains within each of these matrix regions using NanoSIMS measurements of oxygen and carbon isotopes as well as silicon and calcium distributions to distinguish silicates from other presolar grain types.

**Methodology:** We analyzed ALHA77307, a carbonaceous chondrite known for its highly primitive chemistry and low degree of alteration [5].

**SEM Data Collection:** A low-resolution (140 X magnification) context map of the sample was obtained using the JEOL 7900F SEM in the Astromaterials Research and Exploration Science (ARES) division at the NASA Johnson Space Center. Operating conditions

included a 15 kV beam, 4 nA current, and a working distance of 9.0 mm. This map was used to identify target matrix areas for later NanoSIMS analysis. Matrix regions were selected according to the following criteria: (1) 100  $\mu\text{m}$  away from the sample edge, (2) minimal abundances of inclusions (*e.g.*, chondrules, calcium-aluminum inclusions (CAIs), chondrule fragments, and refractory phases) (3) an approximate diameter greater than 50  $\mu\text{m}$ , and (4) little evidence of terrestrial weathering (*e.g.*, calcium-filled veins, cracks, and calcium-encircled chondrules).

Sixteen matrix areas were then mapped at high resolution (1000 X magnification) on the same instrument using the operating conditions previously described. The concentration of magnesium-, aluminum-, sulfur-, and calcium-rich matrix grains within each selected region were measured with an Oxford Instruments Ultim Max SDD X-ray detector to determine which of these were most effective in tracing changes in alteration throughout the matrix on micrometer scales. Differences in the abundance these grains have previously been shown to reflect changes in alteration between different astromaterials [6].

**Matrix Chemistry Analysis:** We used the Oxford Instruments AZtec software and ImageJ software to characterize the concentration of the magnesium-, aluminum-, sulfur- and calcium-rich grains in Energy Dispersive Spectroscopy (EDS) images for nine matrix areas. Iron was ubiquitous within the matrix and therefore not effective for measuring changes in chemistry from alteration on micrometer scales. Small (< 20  $\mu\text{m}$ ) isolated grains from smashed inclusions were considered part of the matrix. Instrumental noise was removed through a combination of 4 tools: remove outliers, despeckle, smoothing, and thresholding. Any remaining outliers were manually subtracted before we calculated elemental abundances in the matrix.

**NanoSIMS Data Collection:** Isotopic analyses of five matrix regions in ALHA77307 were performed with the Cameca NanoSIMS 50L in the ARES division at the NASA Johnson Space Center. We used a 0.8 pA Cs<sup>+</sup> primary beam to collect ion images of <sup>12</sup>C<sup>-</sup>, <sup>13</sup>C<sup>-</sup>, <sup>16</sup>O<sup>-</sup>, <sup>17</sup>O<sup>-</sup>, <sup>18</sup>O<sup>-</sup>, <sup>28</sup>Si<sup>-</sup>, and <sup>40</sup>Ca<sup>16</sup>O<sup>-</sup>. The sample was presputtered with a 200 pA Cs<sup>+</sup> beam, and the scanning speed was adjusted between 4600 and 5400  $\mu\text{s}/\text{pixel}$  such that the total analysis time for each 20  $\mu\text{m}$  x 20  $\mu\text{m}$

image was approximately three hours. Instrumental mass fractionation was monitored by analyses of San Carlos olivine and USGS graphite standards measured with 3.0-3.4 pA of Cs<sup>+</sup> and 1.4-1.6 pA of Cs<sup>+</sup>, respectively.

**Results:** Four of the matrix regions (Area 2, Area 4, Area 13, and Area 15), are greater than 30000 μm<sup>2</sup> in size. Area 18 is ~10000 μm<sup>2</sup> in size. Magnesium abundances vary from 456 ppm (Area 18) to 6838 ppm (Area 13). Aluminum ranges from 73 ppm (Area 13) to 218 ppm (Area 15). Sulfur abundances range from 423 ppm (Area 2) to 2416 ppm (Area 13). Calcium abundances vary from 70 ppm (Area 2) to 2224 ppm (Area 15) (Fig. 1).

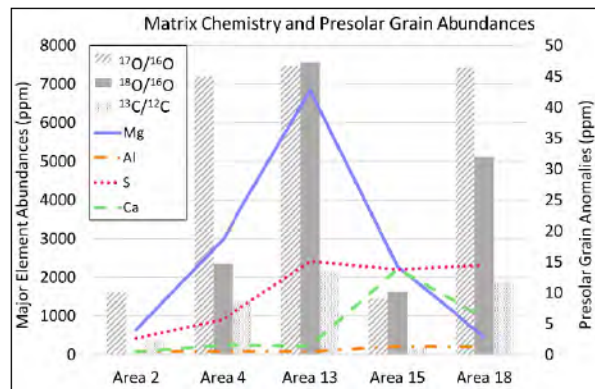


**Figure 1.** Major element matrix chemistry (magnesium, aluminum, sulfur, and calcium) plotted as ppm for each of the five matrix regions in ALHA77307. Corresponding abundances of presolar grains are divided between the ratios in which they have an isotopic anomaly (<sup>17</sup>O/<sup>16</sup>O, <sup>18</sup>O/<sup>16</sup>O, and <sup>13</sup>C/<sup>12</sup>C).

Using NanoSIMS, 147 presolar grains were identified by their <sup>18</sup>O/<sup>16</sup>O, <sup>17</sup>O/<sup>16</sup>O, and <sup>13</sup>C/<sup>12</sup>C oxygen isotope ratio anomalies (Fig. 1). The average presolar grain abundance for the five matrix regions is 331 ppm. Abundances are 233 ppm, 351 ppm, 395 ppm, 360 ppm, and 487 ppm for Areas 2, 4, 13, 15, and 18, respectively. Most grains are <sup>17</sup>O-rich, with some Area 13 grains exhibiting <sup>18</sup>O anomalies consistent with supernova grains (Fig. 2). δ<sup>13</sup>C values range from 823‰ to 25131‰, δ<sup>17</sup>O values range between -775‰ and 3031‰, and δ<sup>18</sup>O values range between -542‰ to 546‰ relative to the meteorite matrix, which is assumed to represent the solar composition.

**Discussion:** In areas more enriched in magnesium-, calcium-, and sulfur-rich grains (three elements whose abundances are useful in determining the extent of matrix alteration), presolar grains abundances show significant variation. Generally, matrix regions with the highest magnesium content also contain the highest abundances of <sup>17</sup>O- and <sup>18</sup>O-rich presolar grains, except for Area 18 (Fig 1.). <sup>18</sup>O-rich grains are present in every region where the sulfur concentration is above 423 ppm.

Among the five matrix areas, the lowest abundances of <sup>13</sup>C-anomalous and <sup>17</sup>O-anomalous grains occur when

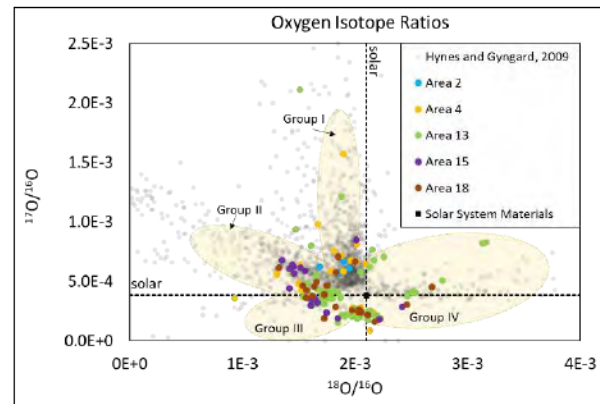


**Figure 2.** Oxygen isotope values for the 147 presolar grain anomalies identified across five matrix regions of ALHA77307. The dotted lines represent solar system oxygen isotope ratios from [7]. Previous presolar grain data is from [8].

sulfur and calcium are present at similar values (< 500 ppm difference). The abundance of <sup>13</sup>C-rich grains then increases with increasing concentration of sulfur where calcium abundances are low. It is important to note that the presolar grain abundance calculations rely on the NanoSIMS-derived anomaly images, which may either overestimate grain diameters due to primary beam effects or underestimate a presolar isotopic anomaly due to matrix grain overlap [9].

The preliminary approach for measuring elemental concentrations within the matrix involved reducing and smoothing each elemental image until small (< 1 μm) outliers and noise were removed from the images. However, this approach underrepresented the surface area of the grains, thus giving inaccurate matrix chemistry results. To improve this approach, the SEM-EDS processing procedure will be revised with fewer applications of the remove outlier tool, a lower threshold for grain removal, and a more robust smoothing procedure to ensure the surface area of the grains rich in targeted elements are fully represented in the dataset. Instrumental noise will then be removed by (1) manually subtraction before calculating the surface area, or (2) removing the artifacts after surface area is calculated. This will more accurately characterize the surface area of the matrix grains enriched in the target elements for comparison with presolar grain populations.

**Conclusion:** To test whether micrometer-scale changes in matrix alteration can be used to locate regions with larger presolar grain populations, we studied the mineral chemistry and presolar grain isotopic anomalies for five matrix regions of

ALHA77307. While preliminary results do not show a direct correlation with the elemental chemistries commonly associated with changes in alteration and presolar grain populations, some trends and relationships were shown, which suggests more extensive study is needed. Through continued studies, SEM-EDS processing methods will also be revised to achieve higher accuracy.

**Acknowledgements:** Thank you to Timmons Erickson for guidance in SEM data collection. This work was supported by the 2023 LPI Summer Intern Program under USRA and the NASA Science Mission Directorate.

**References:** [1] Zinner E. (2014). *Meteorites and cosmochemical processes*, 181-213. [2] Nittler L. R. and Ciesla F. (2016). *Annu. Rev. Astron. Astrophys.*, 53-93. [3] Nagashima K. et al. (2005) LPS XXXVI, Abstract #1671. [4] Floss C. and Stadermann F. (2009) *Geochim. Cosmochim. Acta.*, 2415-2440 [5] Brearley A. J. (1993). *Geochim. Cosmochim. Acta*, 1521-1550. [6] Brearley A. J. (2006) *Meteorites and the early solar system II*, 587-624. [7] Lodders K. (2003). *Astrophys. J.*, 1220-1247. [8] Hynes K. M. and Gyngard F. (2009). LPS 40, Abstract #1198. [9] Nguyen A. N. et al. (2010). *Astrophys. J.*, 166-189.





**INVESTIGATING LUNAR SUBSURFACE CAVITIES USING THERMAL INERTIA AND TEMPERATURE MAXIMUM TO MINIMUM RATIOS.** A. R. Ascione<sup>1,2</sup>, R. A. Slank<sup>1</sup>, G. L. Eggers<sup>1</sup>, <sup>1</sup>Lunar and Planetary Institute (USRA), Houston TX 77058, <sup>2</sup>Department of Earth and Planetary Sciences, Rutgers University, Piscataway NJ 08854 (ara172@scarletmail.rutgers.edu).

**Introduction:** Lava tubes are promising sites for future lunar exploration, as they provide natural shelter from harsh surface conditions. They may serve as cold traps for volatiles and store relatively undisturbed geologic samples of the Moon's subsurface. Lava tubes have also been proposed as future sites for human habitation [1]. Prior studies have investigated the presence of lava tubes and other subsurface cavities on the Moon [2-7], but many likely remain undiscovered. Here, we test the capabilities of thermal inertia (TI) and temperature maximum-to-minimum ratio ( $T_{\text{ratio}}$ ) techniques for detecting subsurface cavities on the Moon, established in a previous study [2].

**Method:** Thermal inertia is the resistance of a material to changes in temperature, and it is largely dependent on thermal mass [8]. A feature with low thermal mass is less resistant to changes in temperature and therefore has low thermal inertia. Such a feature would exhibit higher  $T_{\text{ratio}}$  values than its surroundings since it experiences a wider range of temperature maximum and minimum values.

Lava tubes are linear, roofed channels that form as a result of volcanic activity [9]. The roof above a lava tube has less thermal mass than the surrounding terrain and therefore exhibits a linear, low-TI feature. For  $T_{\text{ratio}}$ , a lava tube will appear as a linear feature with high values.

Lava pits are void spaces that result from lava inflation followed by collapse in either volcanic lava flows [10] or impact melt sheets [1]. These features likely contain more exposed rock than regolith [11].

Since rocky outcrops are more resistant to temperature changes, pits will appear as circular high-TI features and circular low- $T_{\text{ratio}}$  features. Similar signatures will also occur at skylights where part of a lava tube roof has collapsed.

We created a catalog of 37 lava tube, lava pit, and skylight sites identified by other studies [2-7]. Since diurnal temperature data is necessary for calculating TI and  $T_{\text{ratio}}$ , a year (9/25/2015–9/26/2016) of the most recent Lunar Reconnaissance Orbiter's (LRO) Diviner global temperature maps were downloaded from NASA's Planetary Data System (PDS). We checked for diurnal coverage of the 37 target sites during this time interval via automated script. Upon confirmation, albedo, Julian date, and local time maps were downloaded for the appropriate diurnal cycles, as well as a digital elevation model derived from LRO's Lunar Orbiter Laser Altimeter (LOLA). We combined these datasets to calculate and produce TI and  $T_{\text{ratio}}$  maps [8, 12-13]. Finally, we analyzed these maps with ENVI to determine if subsurface cavities could be detected.

**Results/Discussion:** Out of the original 37 target sites, 22 had diurnal temperature coverage available and were able to be investigated. Out of these sites, 1 lava tube and 10 lava pit signatures were clearly discernable in our maps.

A previous study [2] indicated the presence of lava tubes and a skylight at the Highland 1 site, for which we show our TI and  $T_{\text{ratio}}$  maps of this area (Fig. 1). The linear, low-TI signatures (Fig. 1, A) are indicative of the presence of one or more lava tubes. One trends northeast-southwest, and the other trends northwest-

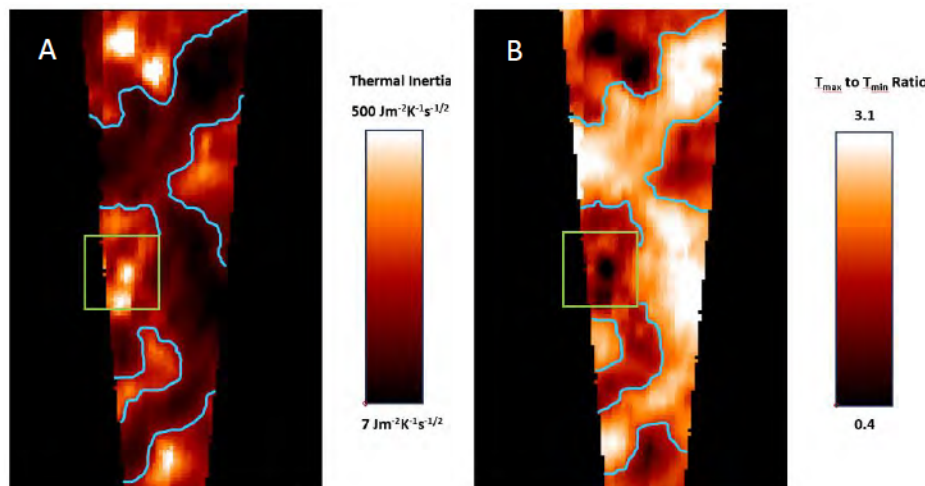


**Figure 1:** A: TI and B:  $T_{\text{ratio}}$  maps of the Highland 1 site using data from the 04/02/2016 to 05/04/2016 lunar diurnal cycle. The brighter colors indicate higher values, while darker colors indicate lower values or missing data. The green box outlines where the skylight is located. The blue outlines lava tube.

southeast. The vertical orientation of the lava tubes cannot be resolved using these techniques. Therefore, these features may intersect, or they may have crossed over each other.

The two linear features were also present in the  $T_{\text{ratio}}$  map (Fig. 1, B). High- $T_{\text{ratio}}$  features appear in approximately the same locations as the low-TI features.

The similarity between feature locations and orientations (Fig. 1) support the claim that one or more lava tubes exist in this area. Our TI and  $T_{\text{ratio}}$  maps of the Highland 1 site also correlate well with those of a previous study [2], who analyzed a different diurnal cycle. This demonstrates the capabilities of both techniques for detecting skylights and lava tubes.

A lava pit was previously detected within Mare Ingenii [3]. In our TI map (Fig. 2, A) of this site, there is a small, circular, high-TI feature where the pit is located compared to its surroundings. However, there is not a linear, low-TI signature near the pit. This indicates that the feature is in fact a pit and not a skylight. The  $T_{\text{ratio}}$  map (Fig. 2, B) supports this, with the feature having a low- $T_{\text{ratio}}$  signature and no presence of a linear feature nearby. The similarity between the locations of high-TI and low- $T_{\text{ratio}}$  values (Fig. 2) add validity that the TI and  $T_{\text{ratio}}$  techniques are effective at detecting and characterizing lava pits.

An earlier study indicates that there is a void space extending at least 20 meters beneath the west wall of the Mare Ingenii pit [4]. Overhanging material should exhibit lower TI than the surrounding material since it has less thermal mass. In Figure 2, the west wall of the pit has lower TI values and higher  $T_{\text{ratio}}$  values, supporting the presence of an overhang.

**Conclusions:** Our results show that lava tubes, skylights, and lava pits are able to be detected and characterized using TI and  $T_{\text{ratio}}$  techniques. It is

important to note that these techniques can only detect these subsurface cavities in the diurnal skin depth ( $\sim 1$  m [14]), since calculating thermal inertia relies on the diurnal temperature change. Any subsurface cavities below this depth will not be detected with these techniques. That said, the results of this study can be further assessed as more temperature data is made available on the PDS.

**Acknowledgements:** This work was supported by the Lunar and Planetary Institute's (LPI's) 2023 Summer Intern Program in Planetary Science and a Cooperative Agreement between NASA's Science Mission Directorate and the LPI, which is operated by the Universities Space Research Association (USRA).

We would also like to thank the NASA-PDS geosciences node, from which DLRE and LOLA datasets were downloaded for this study.

**References:** [1] Walden B. E. et al. (1998) *LPI/TR*, 1, 16-17. [2] Slank R. A. (2016) UTEP M.S. Thesis. [3] Wagner R. V. and Robinson M. S. (2022) *JGR*, 127. [4] Wagner R. V. and Robinson M. S. (2014) *Icarus*, 237, 52-60. [5] Chappaz L. et al. (2017) *Geophys. Res. Lett.*, 44, 105-112. [6] Deran A. et al. (2016) LPS MMXVI, Abstract #2986 [7] Qiu X. and Ding C. (2023) *Remote Sensing*, 15, 2850. [8] Scheidt S. et al. (2010) *JGR*, 115. [9] Neuendorf K. K. E. et al. (2005) *Glossary of Geology (5<sup>th</sup> edition)*, 779. [10] Deschamps A. et al. (2014) *G<sup>3</sup>*, 15, 2128-2150. [11] Bandfield J. L. et al. (2011) *JGR*, 116. [12] Maltese A. et al. (2013) *Hydro. Sci. J.*, 58, 1144-1161. [13] Xue Y. and Cracknell A. P. (1995) *Internat. J. Remote Sensing*, 3, 431-446. [14] Williams, J. P. et al. (2017) *Icarus*, 283, 300-325.

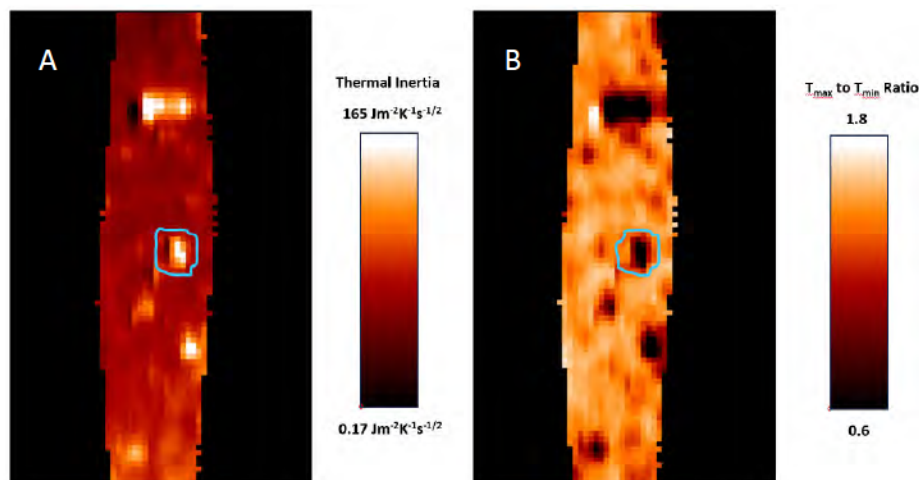


**Figure 2:** A: TI and B:  $T_{\text{ratio}}$  maps of the Mare Ingenii site using data from the 04/02/2016 to 05/04/2016 lunar diurnal cycle. The brighter colors indicate higher values, while darker colors indicate lower values or missing data. The blue circle outlines the detection of the lava pit.

**Stories of CAIs Revealed Through Secondary Processes.** V. E. Burnette<sup>1,2</sup>, P. Mane<sup>1</sup>, and T. Erickson<sup>3</sup>, <sup>1</sup>Lunar and Planetary Institute (USRA), Houston, TX 77085, <sup>2</sup>The University of Texas at Austin, Austin, TX 78705, <sup>3</sup>Jacobs-JTS, NASA Johnson Space Center, Houston, TX 77058.

**Introduction:** Calcium-aluminum inclusions (CAIs) are found in chondritic meteorites, but the largest and most studied CAIs are hosted in carbonaceous chondrites [1]. Thorough study of the mineralogy of these inclusions like those in Allende [2] revealed that their mineral constituents closely matched the predictions of thermodynamic models of the solids that condensed from an extremely hot (>1500 K) gas with a bulk solar composition [3-4]. This was inferred as evidence that CAIs were the earliest solids within the Solar System, and they likely formed about 0.1 to 1 au from the protosun [1,4].

Beyond some overall bulk mineral and isotopic similarities, CAIs exhibit a variety of textures, supporting various evolutionary models. CAI textures coupled with their age constraints provide invaluable insights into the conditions and dynamics of the early Solar System. CAIs condense close to the Sun, however, the accretion region for chondritic meteorite parent-bodies is further away (3.6 to 3.8 au) from the Sun [5]. Therefore, CAIs must travel from their formation region near the protosun to this accretion region. The mechanisms of this transport are debated, but hypotheses such as the X-wind model [6-7] and turbulence model [8] have been proposed to address this. While beyond the scope of this project, the path CAIs take to get to the chondrite accretion region is a key consideration. The nature of their journey could affect how, when, and where the secondary processes in these CAIs occurred [4]. Did secondary processes happen during travel away from the protosun or later during accretion with the parent body? How were the CAIs affected by varying thermochemical processes? I have undertaken an in-depth, descriptive study of the secondary alteration of select CAI samples to better answer these questions.

**Methods:** We chose three CAIs that experienced a range of post-formation processes to gain a better understanding of secondary alteration. The selection was based on previous preliminary electron microprobe data collected to identify mineralogy and chemical composition [9]. The CAI samples were chosen from NWA 5508 (CV3), NWA 12772 (CV3), and Coolidge (CL4) carbonaceous chondrites.

We used scanning electron microscopy (SEM) and electron backscatter diffraction (EBSD) techniques for detailed chemical, mineralogical, and textural analysis of the CAIs. Backscattered electron (BSE) images and maps were taken of Coolidge and NWA 5508 using the Lunar and Planetary Institute (LPI) Phenom SEM. The

NASA Johnson Space Center's JEOL 7900F SEM was used to obtain chemical maps of all samples using energy dispersive spectroscopy (EDS). High resolution EBSD analysis identified the mineral phases and textures, providing key information on their nature in the CAIs. Based on the SEM and EBSD data, minerals of interest were selected for quantitative chemical electron probe micro-analysis (EPMA) using the JEOL JXA-8530F. The EBSD data were processed using Oxford's AZtec Crystal software.

**Results and Discussion:** The EDS maps show that the NWA 5508 and NWA 12772 CAIs designated "Saguaro" and "Hoopoe" respectively [9] are enriched in calcium while the Coolidge CAI designated "Cottonwood" is dominantly aluminum and magnesium rich.

*Saguaro* is a (~1.5cm diameter) igneous Type B CAI with a rounded shape. The dominant phases are melilite, spinel, and Al-Ti pyroxene with minor anorthite. Spinel is subhedral and occurs in clusters. Some of these clusters have a circular geometry which encloses other minerals. These spinel structures are known as palisades (**Figure 1**). Some palisades form near perfect circles while others are more irregular in shape. Melilite in *Saguaro* ranges in size from coarse (>250 $\mu$ m) to fine grained (~5-7 $\mu$ m) and forms intergrown laths. Around a third of the melilite grains exhibit simple twinning about their <001> axis. The Al-Ti pyroxene has a poikilitic relationship with the spinel. Anorthite is the least abundant mineral, is the finest grained (1-20 $\mu$ m on average) and occurs as an interstitial secondary phase. *Saguaro* is surrounded by accretionary rims made of very fine magnesium and sulfur rich matrix material.

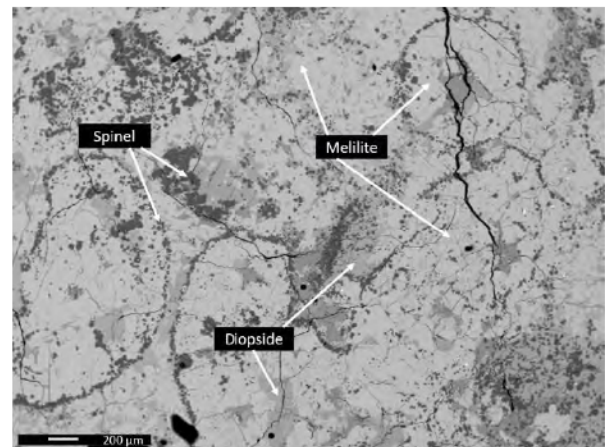


**Figure 1:** BSE image of spinel palisades in *Saguaro*.

The spinel palisades and twinned melilite suggest that Saguaro has an igneous history and experienced minimal thermal metamorphism or aqueous alteration. At some point in time after the initial condensation of the minerals and formation of the inclusion, the sample was remelted and quickly solidified. The formation of the palisades is still heavily debated. One hypothesis is that the palisades are the rims of smaller CAIs that accreted early on, essentially acting as xenoliths within the larger CAIs [10]. Another hypothesis suggests an igneous origin for palisade structures [11-12] wherein the melt traps gas bubbles, and the spinel nucleates on the surface of this bubble. At some point, the bubble bursts as the vapor escapes allowing for the melt to fill in the space left behind [11]. As the melt cools, crystals formed inside and outside the palisades have the same composition. The results of the EPMA analysis help differentiate which hypothesis works better is compatible with this CAI. Based on the chemical data of 41 melilite grains, the composition inside and outside the palisades is nearly identical. Five grains inside the palisades showed slightly higher magnesium concentrations, but do not show any discernible trend. Additionally, there are two grains outside the palisades that also show higher magnesium content. Besides magnesium, no other elemental abundances differ with any significance. This finding indicates that these palisades are likely not exogenous and that they formed from melt-vapor reactions. Our results are consistent with studies by Grossman et al. [11] and Zhang et al. [12].

*Hoopoe* is a ~0.5cm compact Type A CAI with an irregular shape. The dominant mineral phases are melilite, spinel, and hibonite with minor amounts of anorthite, augite, and perovskite. The CAI contains small (<20 $\mu\text{m}$ ) metal nuggets in the bottom right quadrant. The melilite ranges in size from ~500 $\mu\text{m}$  to 50 $\mu\text{m}$ . The larger melilite grains have simple twinning along the <001> axis just like melilite in Saguaro. Melilite in Hoopoe exhibits crystal-plastic strain (**Figure 2**) with misorientation dominantly about the <010> and <110> axes. Spinel shows subhedral to euhedral morphology and appears in clusters. Hibonite is similar to spinel in habit and size, but the grains are more strained. The two minerals are often found together with one appearing to replace the other (**Figure 2**). In some areas, hibonite grains have spinel cores while in other areas, hibonite is surrounded by spinel. Spinel and hibonite show lamellar intergrowth. In those such cases, the <0001> axis of hibonite and the <111> axis of spinel loosely align [13], but in any other scenario there is no relation in orientation. Anorthite is either interstitial or forms a thin rim

around spinel grains. Augite occurs as the outermost layer of the rim sequence after anorthite. Perovskite appears in fine grained recrystallized regions alongside fine augite and spinel and sometimes has a myrmekitic texture.

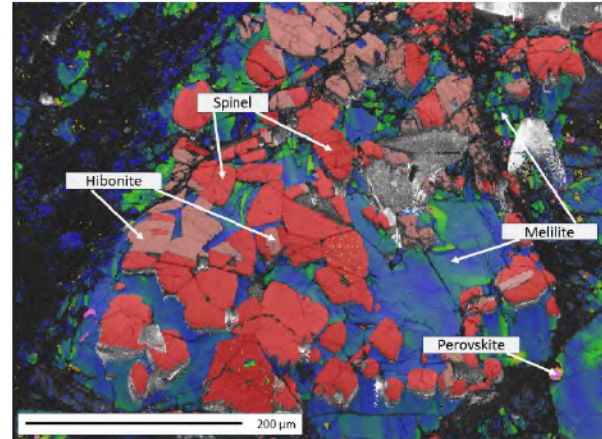


**Figure 2:** Combined EBSD grain rotation orientation distribution (GROD)-Angle map of the deformed melilite and mineral phase map of spinel-hibonite replacement in Hoopoe. The green and yellow domains of the melilite depict higher strain up to 15°.

The abundant strain and deformation features in the melilite and hibonite suggest that Hoopoe experienced shock. This shock could have occurred in the nebula [14] or from an impact of another body on the parent body asteroid. The appearance of fine-grained (<10 $\mu\text{m}$ ) areas of augite, perovskite, and spinel in the dominantly coarse-grained inclusion suggests recrystallization, possibly due to the sudden increase in pressure and temperature. Additionally, there are veins running through the inclusion rimmed by the anorthite and augite which could either be condensation or alteration products.

*Cottonwood*. This ~0.5cm CAI exhibits unique mineralogy and textures that resulted from its high degree of alteration. It is irregular in shape. The dominant mineral phases are spinel and anorthite with minor amounts of augite and rutile. There are trace amounts of fine-grained (<5 $\mu\text{m}$ ) ilmenite. The two main texture types can be seen in **Figure 3**. The first type consists of coarse euhedral to subhedral spinel and anorthite laths. The coarse spinel becomes more anhedral and intergrown in the area around holes forming rims. The second includes fine grained spinel, anorthite, rutile, and iron sulfides. Within these fine regions, the anorthite grains are clustered into domains where they all exhibit the same crystallographic orientation. Rutile exclusively occurs with fine anorthite indicating a potential relationship between

the two. Augite is rare in the core but forms fine grained rims around holes. Cottonwood has a clear and unbroken Wark-Lovering [15] rim (Figure 3) on one side that consists of a sequence of spinel followed by anorthite with augite as the last layer. There is a circular micro-CAI right by the rim containing a spinel core, and anorthite and augite rim, similar to the larger CAI. On the opposite side, the rim is fragmented and broken, and the matrix has infiltrated and mixed with pieces of the inclusion.

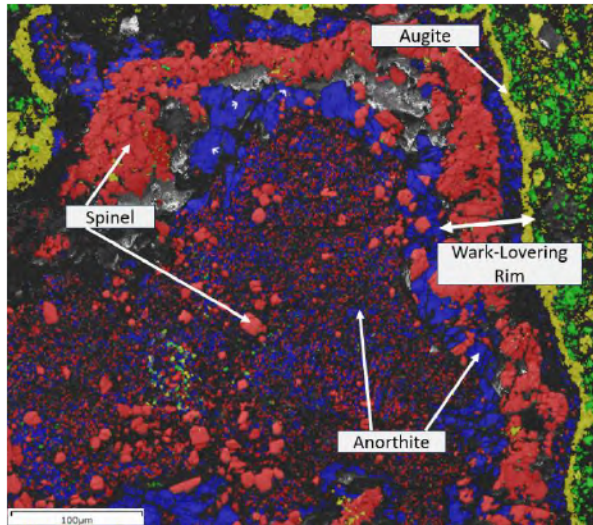


**Figure 3:** Phase map of minerals found in the rim area of Cottonwood. Both the fine and coarse spinel (red) and anorthite (blue) domains are visible. Augite (yellow) separates the CAI from the olivine (green) chondrite matrix.

The abundance of the fine-grained regions full of iron oxides and iron sulfides, secondary phases such as rutile, and oriented anorthite grains is evidence for recrystallization associated with a high degree of metamorphism. Our hypothesis is that rutile formed from a breakdown of a titanium rich phase such as perovskite. We performed EPMA on both coarse and fine-grained spinel to see if the recrystallization included a compositional change. In the data, the fine spinel grains are more enriched in Cr (1-2 wt.%) than their coarse counterparts (0.1-0.5 wt.%). In our interpretation, the metamorphism is responsible for the chemical alteration of the previously refractory inclusion, bringing in the main component elements of chromium and iron as well as sulfur which is moderately volatile. The coarse and fine anorthite grains were also tested for composition change, but the grain size was too small and too intergrown with surrounding phases to get quantitative data. Our data

suggests that the metamorphism in this CAI occurred after the accretion onto the meteoritic parent body.

**Summary and Future Work:** Saguario, Hoopoe, and Cottonwood went through different secondary processing. Saguario melted in the nebula as seen by the twinned melilite and the spinel palisades. The compositional similarity between melilite inside and outside the palisades excludes an exogenous origin for those structures. Hoopoe experienced intense shock which deformed its melilite and recrystallized perovskite, augite, and spinel in fine-grained regions. Cottonwood shows recrystallization consistent with a higher degree of metamorphism after parent-body accretion. Chemical changes occurred along with the textural changes as evidenced by the enrichment of less refractory elements such as sulfur in the recrystallized areas. While this data has provided a wealth of information about these CAIs, there are more avenues to explore. Isotopic analyses could be conducted in order to provide age constraints on these processes differentiating parent body from CAI migration processes.

**Acknowledgments:** We thank Dr. Jenn Gorce, the JXA-8530F microprobe lab manager at NASA Johnson Space Center for her help with conducting EPMA on our samples. This work was supported by the Lunar and Planetary Institute's (LPI's) 2023 Summer Intern Program and LPI's cooperative agreement.

**References:** [1] MacPherson G. J. (2014) *Meteorites and Cosmochemical Processes, Vol. 1 of Treatise on Geochemistry, Elsevier*, 2, 139-179. [2] Grossman L. (1980) *Ann. Rev. Earth Planet. Sci.*, 8, 559-608. [3] McSween H. Y. and Huss G. R. (2021) *Cosmochemistry, Cambridge University Press*, 2, 2-4, 110-121, 142-148. [4] MacPherson G. J. et al. (2005) *ASP Conference Series*, 341, 225-250. [5] Desch S. J. et al. (2018) *American Astronomical Society*, 238, 11. [6] Shu F. H. et al. (2001) *The Astrophysical Journal*, 548, 1029-1050. [7] Desch S. J. et al. (2010) *LPSC*, 41. [8] Cuzzi J. N. et al. (2003) *166*, 2, 385-402. [9] Mouti Al-Hashimi X. (2023) *LPSC*, 54. [10] Lin Y. and Kimura M. (2000) *Geochimica et Cosmochimica Acta*, 64, 23, 4031-4047. [11] Simon S. B. and Grossman L. (1997) *Meteoritics & Planetary Science*, 32, 61-70. [12] Zhang M. et al. (2019) *Meteoritics & Planetary Science*, 54, 5, 1009-1023. [13] Han J. et al. (2022) *American Mineralogist*, 107, 873-884. [14] Mane P. et al. (2022) *Geochimica et Cosmochimica Acta*, 332, 369-388. [15] Wark D. A. and Lovering J. F. (1977) *Proc. Lunar Sci. Conf.*, 8, 95-112.



**MINERAL ASSEMBLAGES IN ESKERS FROM ICELAND: AN ANALOG FOR COLD AND WET ENVIRONMENTS ON MARS.** C. L. De Anda<sup>1,2</sup> and E. B. Rampe<sup>3</sup>, <sup>1</sup>Lunar and Planetary Institute (USRA), Houston, TX 77058, <sup>2</sup>California State University, Long Beach, CA 90815 (candice.deanda01@student.csulb.edu), <sup>3</sup>Astromaterials Research and Exploration Science Division, Houston, TX 77058 (elizabeth.b.rampe@nasa.gov)

**Introduction:** Presently, Mars is a cold and very dry landscape with surface ice at the poles and near-surface ice at mid-to-high latitudes [e.g., 1]. However, there is substantial evidence for glacial and periglacial landforms at mid latitudes, indicating that water ice and glacial activity was once not just confined to the polar ice caps [e.g., 2,3]. Orbital images have revealed several sites with potential esker-like features associated with morphological evidence for glaciers [e.g., 4,5]. These candidate eskers have been estimated to be from the mid-to-late Amazonian period in Mars' history (i.e., 110-330 Ma), which would indicate wet-based glaciation fairly recently in Mars' history [e.g., 4].

Eskers are long, and often, sinuous ridges of sediment that are deposited by meltwater as it flows beneath glaciers and ice sheets in cold and wet environments [e.g., 6]. The deposition of sedimentary facies within these glaciofluvial features and how the sediments are altered by glacial meltwaters are not widely understood, and addressing these topics is critical to characterizing their mineralogical composition, morphological footprint, and sedimentological history. A NASA Solar System Workings grant was awarded to a team of scientists led by Dr. Alicia Rutledge at Northern Arizona University to characterize the morphology, sedimentology, and mineral assemblages of Mars-analog eskers in southeast Iceland [7]. The work presented here is focused on examining the mineralogy and composition of the esker sediments to get a better understanding of their make-up and whether they exhibit certain mineralogical signatures that could distinguish them from other similar sedimentological features on Mars (e.g., inverted channels). Through bulk mineral analysis of eskers of varying exposure ages in a Mars-analog environment, we aim to determine the degree of aqueous alteration experienced by eskers sediments and characterize any mineralogical evolution within eskers with increasing exposure age. This research will ultimately help us piece together more of Mars's geologic history and evolution.

**Methods:** We used X-Ray Diffraction (XRD) for quantitative mineralogical analysis of sediments from four eskers of different exposure ages: "Emerging Esker" was exposed 5 years ago, "Dragon Egg" and "Trollercoaster" 5-10 years ago, and "The Ring" was exposed 60-80 years ago. We also looked at samples

from four different moraines: "Breida", "Jaja", "Husavik", and "Ding Dong".

**Sample preparation.** We separated <1 mm sediment from the bulk sediment samples collected from the eskers. We also performed size separates on samples that exhibited relatively high concentrations of X-ray amorphous material to better constrain the source of the amorphous material. The size separates included: >2 mm, 1-2 mm, 1-0.5 mm, 250-500  $\mu\text{m}$ , 63-250  $\mu\text{m}$ , and <63  $\mu\text{m}$ .

Each sample was micronized to <10  $\mu\text{m}$  for XRD. Some samples were still wet from the field, so they were dried in an oven at 50 °C until no longer damp. All dried samples were then sieved to less than 1 mm, and 2.5 g to 3.0 g were separated for micronizing. This sediment was then placed into a micronizing vessel along with agate micronizing beads and 20 mL of ethanol. The vessel was then sealed and placed into the micronizing mill at medium speed for 15 minutes. The resulting slurry was then poured into a petri dish and 20 more mL of ethanol was used to rinse any remaining sediment from the vessel into the dish. The dish was then placed back into the oven to allow the micronized slurry to dry. Once dry, if there were any leftover visible grains, the sediment was pulverized using an agate mortar and pestle. After all sediment was properly crushed, the micronized samples were then spiked with 20 wt.% corundum as a standard. This standard enables quantification of the X-ray amorphous component.

**X-Ray Diffraction.** After being mixed until homogenized, each spiked sample was loaded as random powder mounts for analysis on the Panalytical X'Pert Pro MPD with a cobalt source. Instrument measurement conditions include: 45 kV voltage, 40 mA current, 2-90 °2 $\theta$  scan range, 0.026° scan step size, and 96 seconds per step. We also used a beam knife to help reduce background at lower angles.

**Pattern Analysis.** The data were analyzed using the program Profex [8]. Each pattern was run with the following crystallographic information files: diopside, quartz, actinolite, chlorite, magnetite, andesine, augite and corundum. Some of the patterns were also fit with olivine, hematite, and chabazite. Most patterns needed to be refined isotropically and occasionally the preferred orientation for andesine was refined.

**Results: Bulk Mineralogy.** The bulk mineralogical data show that all eskers and moraines sampled contain abundant plagioclase and clinopyroxene, with the former being the most abundant mineral in every sample

(Figs. 1-3). All samples also contained quartz, chlorite, and amphibole in smaller amounts. There were also trace amounts of hematite, chabazite, and olivine in most.

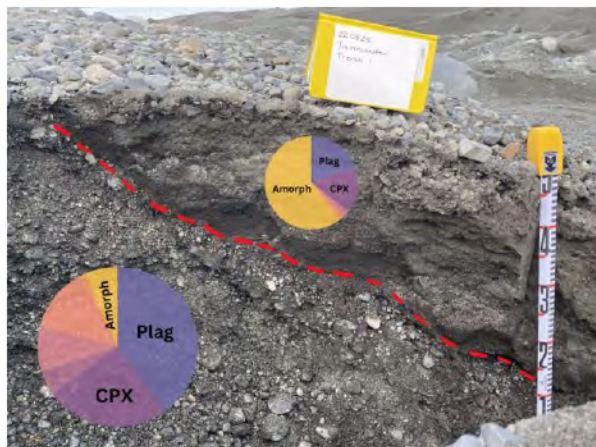


Figure 1. X-ray amorphous material shown in yellow is greatest in the finer facies at the top of the photo versus the coarser facies at the bottom. The dotted red line shows the contact between fine and coarse facies.

The most apparent mineralogical trend in the samples was a higher concentration of amorphous material in the finer facies of the eskers. The finer facies in trench 1 of the Trollercoaster esker has a greater abundance of the X-ray amorphous material than the coarser grained facies (Fig. 1). This trend was also observed in trench samples from Emerging Esker and Dragon Egg.

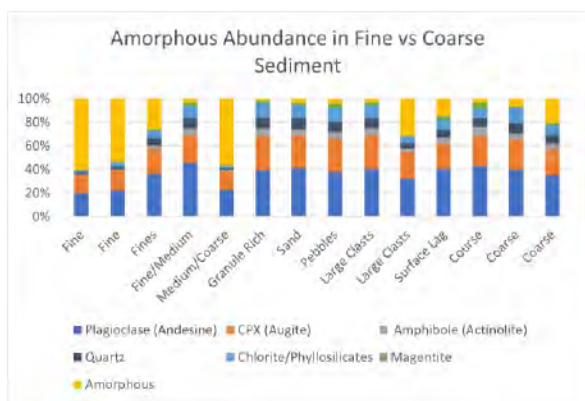


Figure 2. Variation in amorphous abundance (yellow) with grain size. Grain size (y-axis) is based on qualitative field descriptions.

We also find a difference in X-ray amorphous content with the exposure age of the eskers (Fig. 3). Emerging Esker and Trollercoaster have the highest average X-ray amorphous content (30.73 wt.% and 15.62 wt.% for Emerging Esker and Trollercoaster

trenches, respectively). The two trenches through Trollercoaster ~10 m from one another show variation in amorphous content (Trench 1 has an average of 20.51 wt.% and Trench 2, 15.00 wt.%). The Ring, the longest exposed esker, has 9.79 wt.% X-ray amorphous material, and Dragon Egg has 7.40 wt.%. Comparing the average mineral compositions between all four eskers, there is more amphibole, chlorite, and magnetite in the oldest esker. Magnetite shows the greatest relative increase in abundance from the young to oldest eskers.

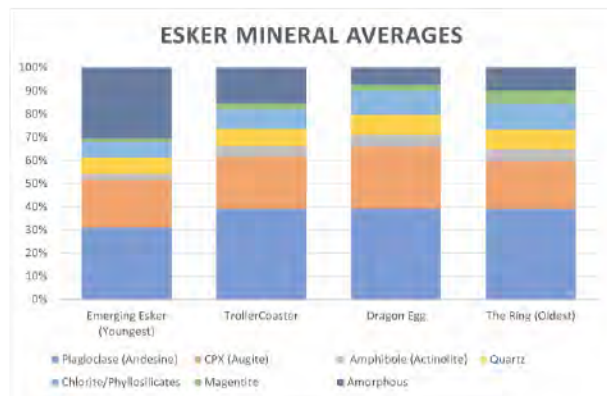


Figure 3. Changes in average mineral content from eskers with different exposure ages from youngest to oldest.

Of the four sampled moraines, Jaja moraine has the greatest abundance of X-ray amorphous material with 54.84 wt.%. Breida and Husavik have similarly high amorphous content with 50.60 wt.% and 48 wt.%, respectively. Ding Dong moraine has the least (22.60 wt.%). We examined size separates of Jaja moraine to help identify the source of the amorphous material.

*Size Separate Analysis.* Analysis of the size separates from samples with higher concentrations of amorphous material demonstrated that the X-ray amorphous material is concentrated in the fine and medium sand-sized sediments. This was evident in all four eskers as well as the Jaja Moraine. The size separates from Trollercoaster Trench 1 showed 36.10 wt.% amorphous material in the >1 mm sediment, whereas the 250–500 μm and the 0.5-1 mm material had 65.15 wt.% and 64.33 wt.%, respectively. The size separates from the Jaja moraine shows a similar trend. The highest concentration of amorphous material is found in the 250-500 μm sediment and the lowest concentration is in the > 2mm with 38.30 wt.%. Two of the Emerging Esker samples also show the highest concentration of amorphous material in the 250-500 μm range.

**Discussion:** Bulk mineralogical data show that X-ray amorphous abundance is highly variable between and within eskers and tends to be concentrated in the



finer facies. The size separates of those finer facies further demonstrate that the X-ray amorphous material is most abundant in the sand-sized sediments, rather than the granule or silt and clay fraction. As such, we hypothesize that the X-ray amorphous material is dominantly primary (i.e., volcanic glass) and is not a secondary alteration product. This volcanic glass may have formed through explosive hydrovolcanism, from lava-ice or lava-groundwater interactions. The relatively low density of this glass may explain the higher amorphous content in the younger eskers, because as the eskers sit exposed over time, the less dense volcanic glass gets transported by seasonal glacial melt water. Alternatively, volcanic glass is susceptible to aqueous alteration [e.g., 9], and the glass in the older eskers (e.g., The Ring) may have been aqueously altered over the course of decades of subaerial exposure.

The fact that amorphous material varies greatly between samples from the same esker also tells us that these eskers are sedimentologically and mineralogically complex and diverse. This was highlighted by the difference in fine vs coarse facies in the two trenches from Trollercoaster. The finer facies in both Trollercoaster trenches have 50-60 wt.% X-ray amorphous material, whereas the coarsest facies have <5 wt.% amorphous material. However, the facies appear to be overall coarser in Trench 2, suggesting that there are differences in depositional environment within an esker at the meter to decameter scale. These differences may be controlled by changes in flow velocity over time of the water that deposited the esker and by the location of the trenches with respect to sinuosity of the esker (e.g., flow velocity on the inside of a curve is greater than on the outside).

The size separates from Jaja Moraine showed a similar mineral and amorphous content as the finer facies in the younger eskers. We speculate that this moraine and the younger eskers share a similar sediment source or that they were deposited contemporaneously from the same subglacial channel.

A general lack of secondary minerals in eskers sediments indicates that water-sediment interactions in these cold and wet environments do not produce substantial amounts of alteration products. Although chlorite is present in most of the sediments, we interpret this mineral as a product of hydrothermal alteration in the source, rather than a product of in-situ alteration in the esker. Hematite and chabazite were identified in some samples near our instrument's detection limit, so additional analysis is needed to confirm their presence. The lack of in-situ secondary minerals in eskers may be explained by insufficient time or it is too cold for these secondary phases to form.

**Implications for Mars:** A goal of this project is to determine whether eskers contain a specific

mineralogical signature that would enable their identification on Mars. Our research demonstrates that eskers do not have secondary phases that we could identify from orbit or on the ground, so secondary minerals cannot be used to identify these features on Mars.

Eskers are sedimentology and mineralogically very complex at the facies scale. We can expect mineral and sediment diversity along the cross section and lengthwise along the esker. These results indicate that a rover on Mars could identify eskers using a combination of sedimentological and mineralogical measurements. Martian eskers may be of interest for future landers because of their implications for liquid water in Mars' recent history. Studying esker sediment composition can teach us about the source region of the sediments without having to go to the source rocks, as they can often be far away or difficult to get to, especially with a rover.

**Future Work:** We will look at amorphous-rich eskers sediments under reflective light microscopy to confirm the presence of glassy particles and to evaluate their relative density by looking for vesicles. Scanning electron microscopy of these glassy particles would further elucidate whether glass is being chemically weathered over time to help explain why younger eskers are enriched in X-ray amorphous material.

A dedicated study to the mineralogy of the cobbles found in eskers and moraines is important to understanding what the source rocks are composed of. Often, the source rocks are difficult to get to or are still covered by ice, so an investigation of the cobbles would be a much easier way to better understand the sources of different facies throughout the eskers.

**Acknowledgments:** This work was supported by the Lunar and Planetary Institute's (LPI's) 2023 Summer Intern Program in Planetary Science and a Cooperative Agreement between NASA's Science Mission Directorate and the LPI, which is operated by the Universities Space Research Association (USRA), and by NASA Solar System Workings grant 80NSSC21K0908.

**References:** [1] Piqueux S. et al. (2019) *GRL*, 46, 14290-14298. [2] Banks M. E. et al. (2008) *JGR – Planets*, 113(E12). [3] Galofre A. G. et al. (2021) *Bull. Am. Astron. Soc.*, 53(4). [4] Butcher F. E. G. et al. (2023) *Annal. Glaciol.*, 1-6. [5] Gallagher C. and Balme M. (2015) *EPSL* 1-2. [6] Storrar R. D. (2015) *ESPL*, 40, 1421-1438. [7] Rutledge A. M. et al. (2023) *LPS LIII*, #2077. [8] Doebelin N. and Kleeberg R. (2015) *J. Appl. Crystall.*, 48, 1573-1580. [9] Gislason S. R. and Arnórsson S. (1993) *Chem. Geol.*, 105, 117-135.



**Mapping and Analysis of Ganis Chasma Rift System, Atla Regio, Venus.** A. T. Gmerek<sup>1,2</sup>, M. B. Weller<sup>1</sup>, and W. S. Kiefer<sup>1</sup>, <sup>1</sup>Lunar and Planetary Institute (USRA), Houston, TX 77058, <sup>2</sup>Department of Geology, University at Buffalo ([andrewgm@buffalo.edu](mailto:andrewgm@buffalo.edu))

**Introduction:** Venus' thick 92 bar atmosphere leads to surface temperatures approaching 737K [e.g., 1]. Omnipresent clouds, comprised of sulfuric acid droplets, obscure the surface from optical telescopes. These conditions make it difficult for landers and probes to return data, radar however is particularly suitable for investigating the Venusian surface. The Magellan mission, launched in 1989, used Synthetic Aperture Radar (SAR) to map 98 % of the surface of the planet [2]. This mission formed our understanding of the surface of Venus and provided imaging of key surface features, such as volcanic rises and rifts [e.g., 2].

Based on the cratering record, Venus' surface is geologically young, with an average age of less than 1 billion years [3]. The majority of volcanic activity occurs in the so-called BAT region, formed by the volcanic rises of Beta, Atla, and Themis Regio, which are thought to be the product of upwelling mantle plumes [4–6]. Hot, rising plumes cause surface uplift, shield volcanism, and deform the lithosphere, leading to rifting. The Devana Chasma rift system is associated with the Beta Regio plume, and Ganis Chasma along with the volcanos Ozza, Maat, and Sapas Mons are associated with the Atla Regio plume.

The Devana Chasma rift system is well-studied and splits into three segments, with the central segment radiating south from Beta Regio and the southern segment radiating north from Phoebe Regio [7]. Ganis Chasma in contrast is poorly studied, with the majority of work focused on rift associated volcanics [8,9]. Ganis Chasma extends radially ~2700 km from Atla Regio initially northward before it turns to a northwest orientation. However, while Devana Chasma is a relatively 'simple' rift system [7], Ganis Chasma is substantially more complex, with multiple rift orientations and complex basin morphologies [10]. Comparable in length rift systems are the ~3000 km long East African Rift (EAR) System on Earth [e.g., 11], or the more than 3000 km long Valles Marineris on Mars [12].

The expression of rifting on Mars occurs by full grabens, with substantial offset on boundary faults on both sides of the rift [12]. In contrast, the continental rifting on Earth (e.g., EAR) occurs predominantly by half grabens, in which there is a boundary fault on only one side of the rift basin and the topography on the other side of the rift is a flexural response to this faulting [11]. Devana Chasma has been identified to be comprised of both half and full grabens [7].

We have assessed the rifting style of Ganis Chasma to determine if rifting on Venus is Earth-like or Mars-like in nature. We have also generated a detailed fault map of Ganis to understand the history of rifting in this region.

**Mapping Ganis Chasma:** Faults within the Ganis region were identified using the Magellan SAR data (150 m/pixel resolution) as well as the altimetry data (10 km/pixel resolution)[2]. The faults identified in the SAR data were overlaid on the 3D topography to determine whether they significantly contributed to the rift morphology. If the fault was less than 12 km long and did not contribute to a visible elevation change within Ganis Chasma, then it was not mapped. Figure 1 shows the significant faults (n=435) within and bounding Ganis Chasma. In addition to the Ganis Chasma fault system, we identified four 'rift splays', that radiate away from the orientation of the main rift. These splays were split up into four groups based on their orientation and groupings, 1 is the southernmost splay and 4 is the northernmost splay. All splay initiation distances are referenced to the southernmost tip of Ganis Chasma. Splay 1 begins at ~935 km and extends 593 km in the N63°E direction. Splay 2 begins at ~1050 km and extends ~158 km in the N3°E direction. Splay 3 begins at ~1200 km and extends ~752 km in the N29°E direction. Splay 4 begins at ~1265 km and extends ~201 km in the N7°E direction. Faults in the Nokomis Montes highlands are cross-cut by the Ganis Chasma faults, suggesting that the Nokomis Montes highlands are older.

In addition to the Ganis Chasma rift, we mapped other nearby features, including three tesserae, three impact craters (Sitwell, Bashkirtseff, and Sidney Craters), a parabolic ejecta deposit surrounding Sitwell Crater, a lava flow emanating from Yolkai-Estsan Mons, two lava flows within the southern segment near Ozza Mons, two volcanic pancake domes, a dike for reference, and three to four shield plains (Fig. 1). Tesserae units are identified by at least two sets of intersecting deformation structures as well as being topographically raised[13]. The impact craters were

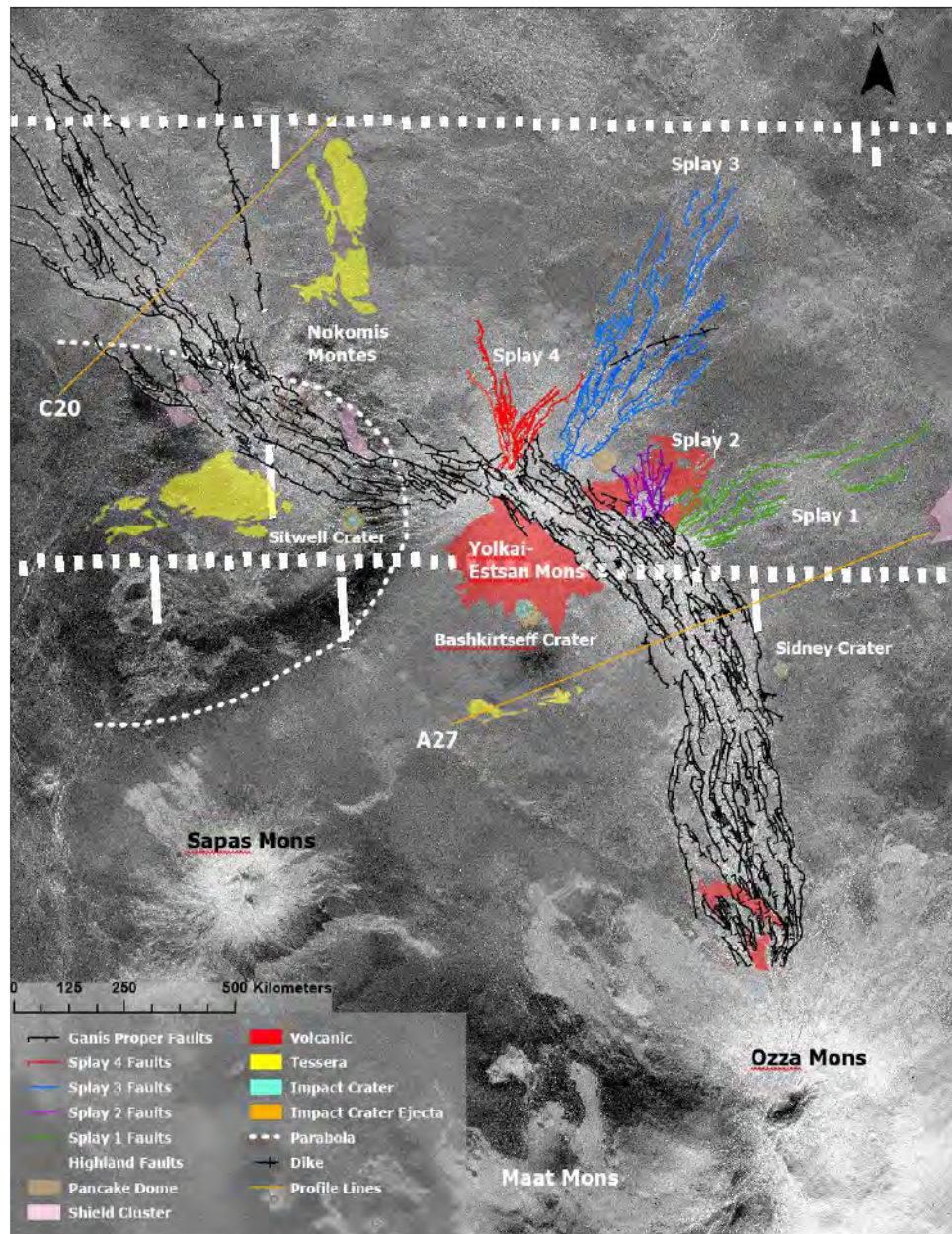


Fig. 1. Map of Ganis Chasma Rift System. Tesserae and Shield plains units were mapped in following the unit descriptions of [13]. Mapping was done in ArcGIS Pro v3.1.1

mapped in two parts, the impact basin and the ejecta blanket. The crater rim was determined from the SAR data and changes in surface roughness and slope. The ejecta was mapped based on the change in radar brightness compared to the surrounding material. The parabola was mapped by following the radar dark material near Sitwell crater. The lava flows were mapped based on the change in radar brightness and morphology, which follows a typical lobate shape. The pancake domes were mapped with SAR, they are classified as prominent circular features with flat tops and a raised rim. The shield plains were mapped based

on an area having an increased amount of raised domes (~1 km - ~10 km diameter) that are interpreted to be shield volcanoes[13].

**Rift Profiles and Basin Morphology:** Utilizing 106 profiles taken an average of every 25 km along the strike of the rift [10], we assessed whether there was similar amounts of normal fault offset on the two sides of the rift basin (a full graben, Figure 2A) or if there was prominent faulting on only one side of the rift basin with a flexural arch on the other side (half graben, Figure 2B).

On Earth, Cenozoic rifts are relatively narrow half graben such as the EAR System which is up to ~60 km wide [11,15]. On Venus, Devana Chasma is a mixture of full and half graben that is up to 300 km wide. [7]. Ganis Chasma is a mixture of full and half graben as well and is up to 360 km wide. In the southern end of Ganis Chasma, which is closest to the plume, the rift is predominantly comprised of full graben. The relative proportion of half graben increases as with distance along the strike of the rift. There are also multiple polarity shifts within Ganis, with the boundary fault occurring on the east side of one basin and then on the west side of the adjacent basin. Polarity reversals are common in terrestrial continental rifts and are also seen in parts of Devana Chasma.

Near the topographic rise in Ganis the rift is mainly full graben. Before the first change in orientation of the Ganis Chasma rift, the average rift depth is 3.75 km and the average rift width is 219 km. The first change in orientation of the Ganis Chasma rift occurs ~900 km from the topographic rise, turning westward towards and through the Yolkai-Estsan Mons volcanic center and associated flows. The four rift splays initiate near this change in orientation, and are potentially radial to, and surround, a portion of this volcanic center (North flank, Figure 1).

Following the first orientation change, the rift begins to alternate between full and half graben. The average rift depth shallows to 2.57 km and the average rift width narrows to 133 km, a change of ~1.2 km and 88 km, respectively. As the rift begins to reorient and alter its strike at ~1900 km, the rifting zone widens to 272 km. This corresponds to rift propagation into the Nokomis Montes highlands. After the second major reorientation the rift zone becomes dominated by half graben. The average rift depth increases to 1.82 km and the average rift width increases to 226 km.

In summary, Ganis Chasma shows both similarities (polarity reversing half graben) and differences (wider, and the presence of full graben) with terrestrial continental rifts. We are currently assessing the implications for rift formation and lithospheric structure on Venus.

**Acknowledgments:** This work was supported by NASA through the Lunar and Planetary Institute (LPI) during the 2023 summer intern program. The LPI is operated by Universities Space Research Association (USRA) under a cooperative agreement with the Science Mission Directorate of NASA.

Magellan radar and topography data was retrieved from the Planetary Data System (PDS) data to generate the results shown. We thank Thea McKenna for her previous work obtaining the 106 profile lines along Ganis Chasma.

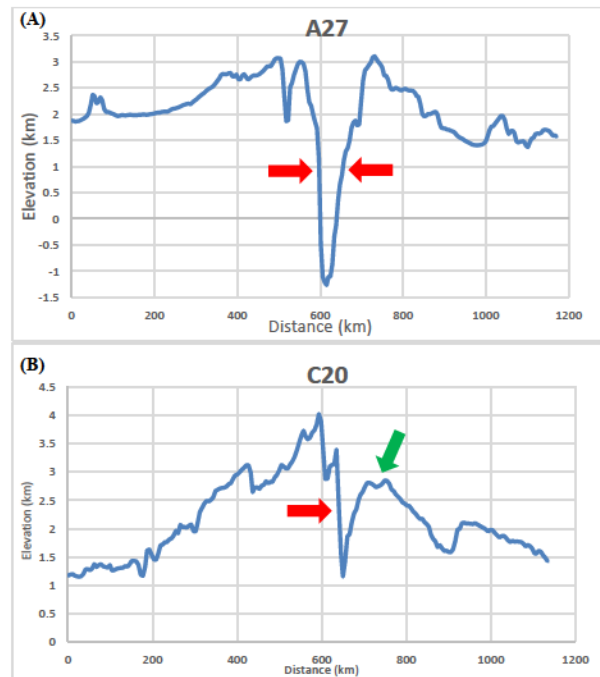


**Fig. 2** Examples of a (A) full graben and (B) half graben within the rift (profile transects indicated on Figure 1). A full graben exhibits two bounding faults (red arrows) with near equal offset; whereas a half graben is controlled by a master fault (red arrow) and the opposite flank exhibits a passive flexural response (green arrow).

**References:** [1] O'Rourke, J.G., Wilson, C.F., Borrelli, M.E. *et al.* (2023) *Space Sci Rev*, 219, 10 [2] Ford, P.G., Pettengill, G.H. (1992) *JGR*, 97, 103-114. [3] Strom, R.G., Schaber, G.G., Dawson, D.D. (1994) *JGR*, 99, 10899-10926 [4] Smrekar, S.E., Kiefer, W.S., Stofan, E.R. (1997) *Venus II: Geology, Geophysics, Atmosphere, and Solar Wind Environment*, (pp. 845-868). Tucson: Univ. of Ariz. Press [5] Robin, C.M.I., Jellinek, M., Thayalan, V., *et al.* (2007) *Earth and Planetary Science Letters*, 256, 100-111 [6] Senske, D.A., Schaber, G.G., Stofan, E.R. (1992) *JGR*, 97, 13395-13420 [7] Kiefer, W.S., Swafford, L.C. (2006) *Journal of Structural Geology*, Volume 28, Issue 12, 2144-2155 [8] Brossier, J., Gilmore, M.S., Head, J.S. (2022) *GRL*, 49, e2022GL099765 [9] Shalygin, E.V., Markiewicz, W.J., Basilevsky, A.T., *et al.* (2015) *GRL*, 42, 4762-4769 [10] McKenna, T.E., Weller, M.B., Kiefer, W.S. (2023) 54<sup>th</sup> LPSC Abstract #2806 [11] Morley, C.K., Nelson, R.A., Patton, T.L., *et al.* (1990) *AAPG Bulletin*, 74 (8), 1234-1253 [12] Schultz, R.A., Lin, J. (2001) *JGR*, 106, 16549-16566 [13] Ivanov, M.A., Head, J.W. (2015) *Planetary and Space Science*, 113-114, 10-32 [14] Ivanov, M.A., Head, J.W. (2011) *Planetary and Space Science*, 59, 13, 1559-1600.



## RAY'S OF SCHRÖDINGER IMPACT EJECTA AND IMPLICATIONS FOR CRATERING PROCESSES.

D. P. Kallenborn<sup>1,2</sup> and D. A. Kring<sup>1</sup>, <sup>1</sup>Lunar and Planetary Institute (USRA), Houston, TX 77058, <sup>2</sup>Earth Science and Engineering, Imperial College London, London SW7 2BP, UK, (danielle.kallenborn20@imperial.ac.uk).

**Introduction:** The ~320 km Schrödinger basin on the lunar farside is the best-preserved basin of its size on the Moon. It is also within the oldest and largest basin on the Moon, the South Pole-Aitken basin, making it a compelling site for geologic studies and lunar exploration [1, 2]. The Schrödinger basin is surrounded by a continuous ejecta blanket (Fig. 1a), albeit one modified by a few younger impact craters, producing an irregular margin. Three long radial canyons and bounding ejecta extend from the crater [1]. Such radial features are produced by a secondary impact process as ejecta from the basin re-impacts the surface. The canyons were carved by chains of individual impact craters [5]. The products are Vallis Schrödinger (260 km long), Vallis Planck (860 km long), an unnamed canyon (80 km long), and several other less-distinct linear features.

While the geology of the Schrödinger basin interior has been studied in the past (e.g., [6-8, 1, 9-11]), little is yet known about the secondary crater chains. Studies of crater chains around other impact basins suggest that the shape and orientation of crater rays can be an effective constraint for determining the processes of the primary impact event [12-14]. The orientation of the rays can be used to infer impact angle and bearing of the primary impactor [13]. The sizes of individual craters within a chain provide information about the sizes of the secondary impactors and energy required to form the canyons.

In this contribution we measured the Schrödinger basin crater rays and their individual craters. We then used these measurements to establish constraints on the primary impact event.

**Methods:** The LROC QuickMap lunar visualization tool was used to evaluate crater morphology and measure distances. Multiple types of data were accessed: Wide-angle camera (WAC) images (100 m/px); narrow-angle camera (NAC) images (0.5 to 2 m/px); NAC region of interest (ROI) mosaics in the Lunar Globe (3D) view; and terrain elevation and slope derived from the Lunar Orbiter Laser Altimeter (LOLA - SLDEM2015 (+LOLA)) [15]. A QuickMap arc tool and an automatically produced elevation transect (SLDEM2015 (+LOLA)) were used to take three rim-to-rim diameter measurements of each crater. Crater shape and final diameter were then represented with a circle tool.

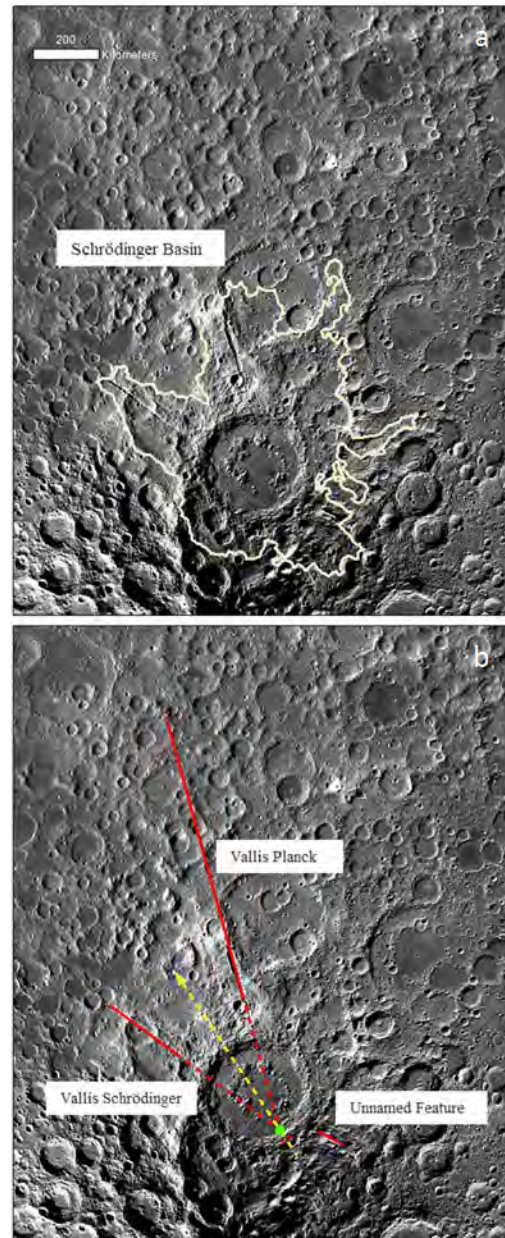


**Figure 1.** Azimuthal Equidistant Projection of the Moon LRO LROC WAC Global Morphology Mosaic 100m v3 (100 meters/pixel) [3], centered on the Schrödinger basin (75°S, 132.5°E). (a) The Schrödinger basin and its continuous ejecta blanket (redrawn after [4]). (b) Three radial secondary features extend from the basin. The two main features Vallis Schrödinger and Vallis Planck intersect close to the southern rim of the basin (green point). The size of the point indicates the uncertainty. The projected bearing of the primary impactor (yellow) runs through the point of intersection and the basin center. A third unnamed feature extends in an uprange direction.

For each crater in the rays, we determined the distance to (a) the Schrödinger basin center, (b) the intersection point with an inferred transient crater rim [2] on that trajectory, (c) the intersection point of the two largest crater rays (Fig. 1b), and (d) the intersection point with the transient crater rim on this trajectory. The procedure accounts for all possible ejection points and, therefore, brackets secondary ejecta velocities. For visualization of the results we used ArcMap (v. 10.5.1).

**Results:** Vallis Planck is significantly longer (860 km) and wider (27 km) than Vallis Schrödinger (260 km and 20 km). With a maximum depth of 2.6 km, the crater ray is also deeper than the Grand Canyon (Fig. 2).

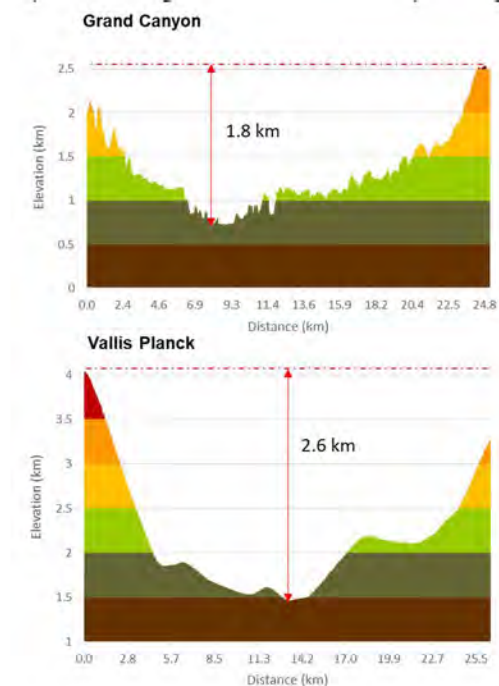


**Figure 2:** Comparison of the width and depth of the Grand Canyon (along the Bright Angel hiking trail from the southern to the northern rim) and Vallis Planck. Colors show 500 m elevation steps but do not represent the same absolute terrain height. Note the different distance scales.

Along the length of Vallis Schrödinger we identified 14 individual craters with diameters between 10 and 16 km, clearly defined by their eroded but still visible crater rims. The craters are partly overlapping and superposed by younger craters. Vallis Planck is not everywhere defined by discernable secondary craters and appears to be modified by the collapse of canyon walls (Fig. 3), which is also apparent in a transect (Fig. 2).

Crater rays present a unique opportunity to calculate impact velocity using measured distances between the secondary craters and their ejection point in a ballistic formula for a curved planetary surface. We considered three possible ejection and impact angles: 20°, 30°, and 45° (Table 1). Maximum ejection velocities for Vallis

Planck are higher than those of Vallis Schrödinger, because of the longer distances covered.

**Table 1:** Maximum ejection velocity for the two main crater rays, assuming an impact at the farthest point along the crater ray, measured from the intersection point of the two rays.

	Vallis Schrödinger	Vallis Planck
20 degrees	1.05 km/s	1.28 km/s
30 degrees	0.97 km/s	1.23 km/s
45 degrees	0.95 km/s	1.25 km/s

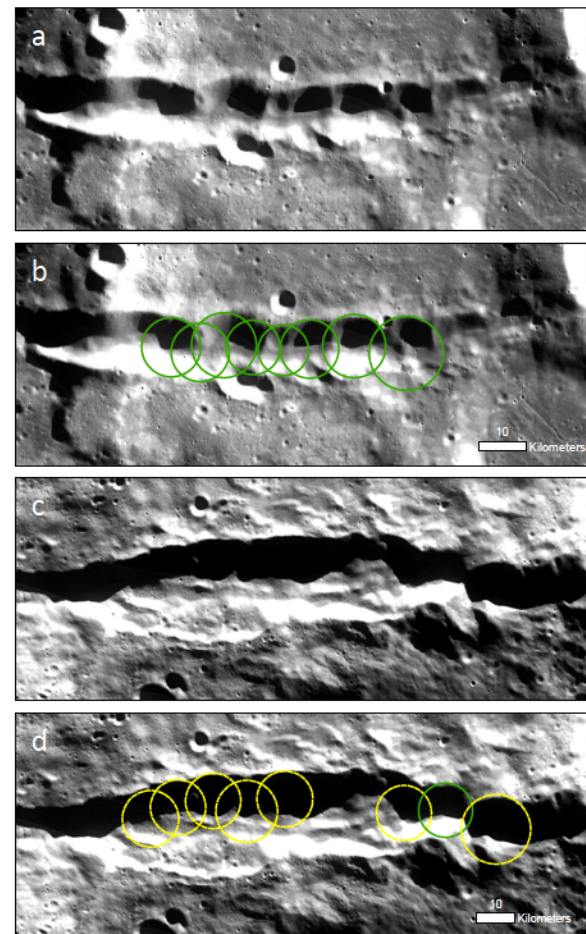


**Figure 3:** Section of Vallis Schrödinger (a and b) and Vallis Planck (c and d) without and with identified craters. Green craters are clearly defined by their eroded crater rims, while yellow craters can only be inferred from the terrain and are not included in the crater scaling calculations.

Calculated secondary impact velocities and the diameters of each crater were then used with an analytical scaling relationship for dry sand [16, 17] assuming anorthositic norite material with a density of 2660 kg/m<sup>3</sup> [18] and a gravity-dominated impact



regime, to determine the sizes of impactors (Fig. 4) and kinetic energy that produced the secondary craters.

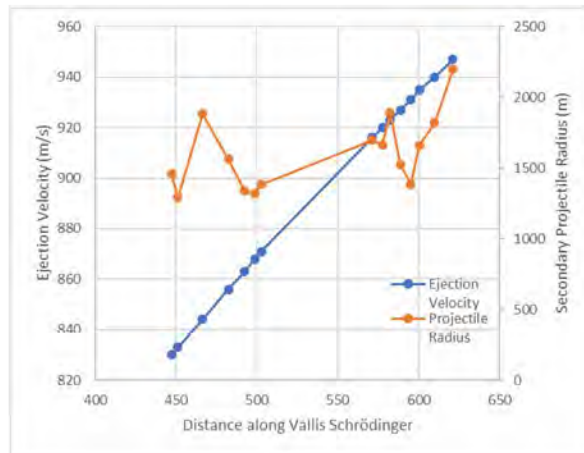


**Figure 4:** Ejection velocity (blue) and projectile radius (orange) for identified craters along Vallis Schrödinger for a 30 degrees ejection angle. The distance is measured from the intersection point of the two rays to the secondary crater. Vallis Planck data falls along the same ejection velocity curve but to greater distance.

Radii of material producing Vallis Schrödinger, considering all possible ejection angles, range from 1.1 to 2.6 km. For Vallis Planck, secondary ejecta radii are generally smaller with most of them being <1 km. There is no systematic increase or decrease in projectile size as a function of ejecta distance. However, this could be caused by sample bias and the age of the features, because smaller craters farther away from the Schrödinger basin are less likely to be well-preserved and identified as part of the crater rays.

**Discussion:** The rays are asymmetrically distributed around the crater and do not converge at the basin center. The bearings of Vallis Schrödinger and Vallis Planck converge at 78.21947°S, 143.71996°E, which is likely the point of first impact [12]. A line from that point through the basin center suggests a SSE to NNW bearing (33.5° west of north; Fig. 1b).

A distributed impact zone may imply a relatively low primary impact angle [19, 20, 12, 13]. Likewise, it may imply relatively low angles for secondary ejecta, ranging from 20 to 45° [13]. Such low angles may produce elliptical secondary craters [21]. While some secondary craters along the two main crater rays could be interpreted as elliptical, a definitive verdict about their shape is difficult due to interference between ejecta curtains produced by simultaneously made secondary craters [22] and subsequent erosion.

The minimum kinetic energy necessary to produce measured craters along Vallis Schrödinger is  $3.41 \times 10^{15}$  kJ. Assuming a similar distribution of excavating impacts along the entire crater ray implies a total kinetic energy of  $6.89 \times 10^{15}$  kJ. Values for Vallis Planck are less

well constrained, but likely higher because of its greater length.

**Conclusions:** The well-preserved Schrödinger basin crater rays provide an opportunity to calculate the velocity of secondary impactors, the size distribution of those impactors, and kinetic energy that excavated the rays. The orientation of the rays also implies a primary impact bearing of 33.5° and an impact angle <45°.

**Acknowledgments:** We would like to thank Gareth S. Collins, Julie D. Stopar and the 2023 Lunar Exploration Summer Interns for their help with this project. We acknowledge the use of imagery from Lunar QuickMap (<https://quickmap.lroc.asu.edu>), a collaboration between NASA, Arizona State University & Applied Coherent Technology Corp. Planetary Data System (PDS) data was used to create the figures. This work was supported by the LPI's Summer Intern Program and LPI's cooperative agreement.

**References:** [1] Kramer, G.Y. et al. (2013) *Icarus*, 223(1), 131-148. [2] Kring, D.A. et al. (2016) *Nature Communications*, 7(1), 13161. [3] Planetary Data Systems (PDS) Cartography and Imaging Sciences (IMG) (2018) Lunar Reconnaissance Orbiter. [4] Fortezzo, C.M. et al. (2020) *51st Annual Lunar and Planetary Science Conference*, 2326, 2760. [5] French, B.M. (1998) *Traces of catastrophe: A handbook of shock-metamorphic effects in terrestrial meteorite impact structures*. [6] Shoemaker, E.M. et al. (1994) *Science*, 266(5192), 1851-1854. [7] Bunte, M.K. et al. (2011) *Geological Society of America Special Paper*, 483, 533-546. [8] Mest, S. (2011) *Geological Society of America Special Paper*, 477, 95-114. [9] Potts, N. J. et al. (2015) *Advances in Space Research*, 55(4), 1241-1254. [10] Steenstra, E. S. et al. (2016) *Advances in Space Research*, 58, 1050-1065. [11] Kring, D.A. et al. (2021) *Advances in Space Research*, 68(11), 4691-4701. [12] Schultz, P.H. and Crawford, D. (2014) *Lunar Plant. Sci. XL*, Abstract #1691. [13] Schultz, P.H. and Crawford, D.A. (2016) *Nature*, 535(7612), 391-394. [14] Guo, D. et al. (2018) *Journal of Geophysical Research: Planets*, 123(6), 1344-1367. [15] Barker, M. K. et al. (2016) *Icarus*, 273, 346-355. [16] Schmidt, R.M. and Housen, K.R. (1987) *International Journal of Impact Engineering*, 5(1-4), 543-560. [17] Holsapple, K.A., (1993) *Annual review of earth and planetary sciences*, 21(1), 333-373. [18] Kiefer, W.S. (2012) *Geophysical Research Letters*, 39(7). [19] Pierazzo, E. and Melosh, H.J. (2000) *Annual Review of Earth and Planetary Sciences*, 28(1), 141-167. [20] Anderson, J.L. et al. (2003) *Journal of Geophysical Research: Planets*, 108(E8). [21] Elbeshausen, D. et al. (2013) *Journal of Geophysical Research: Planets*, 118(11), 2295-2309. [22] Oberbeck, V.R. and Morrison, R.H. (1974) *The Moon*, 9(3-4), 415-455.



**STANDARDIZING A METHOD FOR CREATING A MULTILAYERED REGOLITH SIMULANT TESTBED.** C. G. Locke<sup>1,2</sup>, R. N. Kovtun<sup>3</sup>, T. J. Barrett<sup>1</sup>, and J. E. Gruener<sup>4</sup>, <sup>1</sup>Lunar and Planetary Institute/USRA, 3600 Bay Area Blvd., Houston, TX, 77058, <sup>2</sup>Colorado School of Mines, 1500 Illinois St., Golden, CO 80401 (E-mail [chloelocke@mines.edu](mailto:chloelocke@mines.edu)), <sup>3</sup>Jacobs/NASA-Johnson Space Center, 2224 Bay Area Blvd, Houston, TX 77058, <sup>4</sup>NASA-Johnson Space Center, 2101 E NASA Pkwy, Houston, TX 77058.

**Introduction:** In preparation for lunar exploration in the upcoming years, it is important to understand the properties of the lunar regolith in order to ensure maximum efficiency in our technologies. With a limited amount of lunar regolith samples and few missions (Apollo 15, 16, Luna 17, 21) taking geotechnical measurements of the regolith, simulants are required for large-scale testing. Testing geotechnical properties such as the minimum (least possible amount of compaction), maximum (maximum compaction), and relative densities [1] of regolith simulants is important, as they can be used to calculate the shear strength and bearing capacity, which is vital for surface trafficability or building permanent structures on the lunar surface. Studies have been done testing these factors on simulants (e.g. [2-3]), but with different methods for testbed development. Without a standardized way to create testbeds for these experiments, however, it is difficult to compare the results of the different studies. The goal of this project is to bridge that gap and create this standard on the basis of creating a density profile similar to that on the lunar surface.

**Methods:** The tools used for the experiments included a Gilson ASTM standard mold [1, 4], a clear tubular apparatus designed in collaboration with the team at the NASA Johnson Space Center Simulant Development Lab (SDL) for these experiments, and a model V-51-D1 Syntron Vibrating Table of 115 volts and 60 Hz. The simulant, CSM-LHT-1, was used for all experiments as the anorthositic components have grain sizes up to 1 mm.

Density profiles were created using a layer-by-layer method. Density testing and standardization was first done for the bottom layer before adding a second top layer. The ASTM standard container of a known volume was filled by gently shaking (termed ‘snowing’ [2]) simulant in order to minimize initial compaction. The container was filled to just above the rim, and excess material was scraped off and leveled using a straight edge, allowing for a more precise volume. It was then weighed and placed on the vibration table. For the sake of comparison, all the experimental results shown were tested using a mass of 3.1 kg of simulant. The testing parameters altered throughout the first part of the experiment were vibrational power and the time of compaction. The experiment was limited to a power

of either 310.5 W or 362.25 W as the vibration had to be powerful enough to overcome the inertia of the container yet not too powerful as to move the container itself.

The experiments were run by choosing a power setting and vibrating the material for set number of time (5 or 10 minutes). Data was collected at intervals of 30 seconds or 1 minute. The change in height between the top of the container and the height of the material was used to calculate the new relative density by volumetric change. A minimum of nine tests were conducted at each power setting used.

For the second layer of the model, the transparent polycarbonate (Fig. 1) container was used which allowed for thicker layers and the ability to visually differentiate differences between layers. For these experiments the bottom layer was first compacted to maximum density before ‘snowing’ in the second layer as it was the best way to clearly see the layering. The tests were conducted under the same conditions except for not filling the container all the way to the top, tamping the top of the bottom layer to create a flat surface, and using a funnel to get more even edges for the top layer. The tamping of the bottom layer has been done for all the two-layer tests, and it has been found to not impact the density of the bottom layer.



**Figure 1:** *Top layer experimental model*

A key factor in ensuring accurate measurements using this method is to mark the boundary between the top and bottom layers as it becomes more difficult to distinguish the top layer as it becomes more compacted.

**Results/Conclusions:** Two-layer density profiles are presented in Figures 3 and 4.

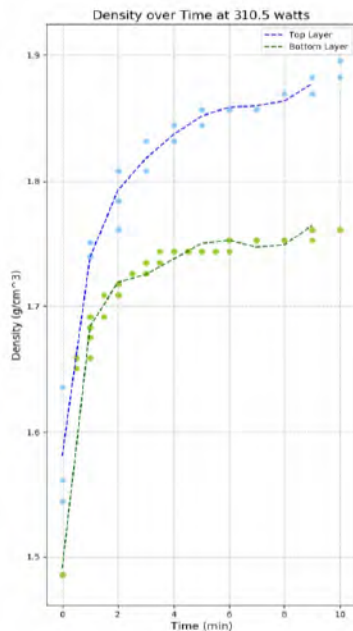


**Figure 3:** Two-layer results at 310.5 watts

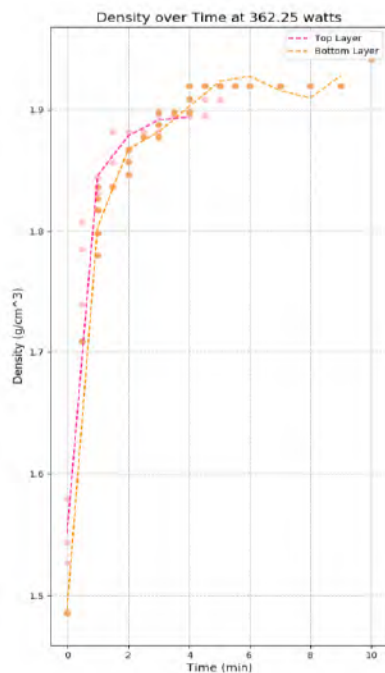


**Figure 4:** Two-layer results at 362.25 watts.

Each graph represents ~ 90 measurements. As displayed in Figures 3 and 4, the method demonstrates a high level of reproducibility for density profiles.

In all the tests conducted, the greatest change in density occurred in the first three to four minutes of the experiment. After that, the density values increased

minimally and oftentimes leveled off. The biggest differences between compacting the simulant at 362.25 W versus 310.5 W is the ability to achieve maximum density. As shown Figure 3, the single layer test, when compacted at 310.5 watts, never reaches maximum density of ~ 1.9 g/cm<sup>3</sup>, however, the two-layer tests, when compacted with the same power, does. Although this may seem counterintuitive, the measurements were consistent across multiple tests. This leads to the possible conclusion that as seen in both Figures 3 and 4, that maximum density in two-layer tests is achieved sooner than their single-layer counterparts.

From the figures, the rate of change in density was calculated and used to test reproducibility by selecting specific densities and attempting to recreate them under specific conditions. For each of these tests, the density found has fallen within  $\pm 5\%$  of the target. With the success of these tests as well as the creation, although limited, of visible layering within the density profile (Fig. 5), simulant testbeds more similar to the conditions on the lunar surface can now be made. In the future, more work is to be done including, taking geotechnical measurements to draw comparisons of shear strength and bearing capacity throughout the density profile, recreating these methods on a larger scale, and using CT scanning to further test the accuracy.



**Figure 5:** Image highlighting the distinction between top and bottom layers.

**Acknowledgements:** We would like to acknowledge Chandler Lawson for help with the construction of our apparatus.

**References:** [1] ASTM Standard D4253 (2006). [2] J. Mantovani et al. (2022) *NASA TM-20220013110*. [3] Long-Fox J. M., et al. (2023) *Ad. Space Res.* 71, 5400-5412. [4] ASTM Standard D4254 (2006).

**Developing a Rapid 16s rRNA Sequencing Protocol for Bioremediation of Martian Regolith for Sustainable Agriculture.** K. Malo<sup>1,2</sup>, K. Lynch<sup>1</sup>, J. Lopez<sup>1,3</sup>, A. Simpson<sup>4</sup>, R. Loureiro<sup>5</sup>, Lunar and Planetary Institute (USRA), Houston, TX 77058, <sup>2</sup>Carleton University, Ottawa, ON K1S 5B6 (kyla.malo@carleton.ca), University of Houston-Clear Lake, Houston, TX 77058, Jet Propulsion Laboratory, Pasadena, CA 91109, Winston-Salem State University, Winston-Salem, NC 27110.

**Introduction:** Mars offers many potential challenges for plant growth and sustainable agriculture [1,2,3]. Martian regolith has very low organic content, potentially low nutrient bioavailability, potentially high heavy metals in bioavailable states, and high perchlorate concentrations [1,2,3,4,5]. Earth-based resupply missions have long turnaround times (2-3 years) which is unsustainable and economically challenging for martian settlements, hence In-situ Resource Utilization (ISRU) of the martian regolith will be required to help develop bioregenerative (i.e. closed-loop) life support systems and food supplies [1,2,6].

Bioremediation of martian regolith is the most promising method to create stable soils capable of providing a suitable habitat for plant-microbe interactions and allowing for healthy crop growth [4,5,7,8]. Perchlorate mitigation can be performed using perchlorate reducing microbes [5,7,8]. To offer the best chance of active perchlorate reduction, an established microbial consortia from perchlorate rich soils in the Pilot Valley Basin, Utah, [9] will be used to inoculate the Martian regolith simulants. The addition of a microbiome capable of perchlorate reduction and bioremediation is expected to reduce the amount of perchlorate to safe levels, increase the organic content, and increase some of the necessary nutrient bioavailability [4,5,7,8].

To test the success of the bioremediation efforts, changes in key nutrients (N, P, K, C, etc.), pH, and perchlorate concentrations will be measured regularly. However, since the microbiome is what is exerting these changes on the simulants, it is important to measure the changes occurring in the microbiome regularly as well. To do so, the development of a sequencing protocol capable of rapidly identifying the microbial species and their relative abundances in the Martian regolith simulants microbiome was necessary.

**Methodology:** The Oxford Nanopore Technologies MinION MK1b was the sequencer used for this project. The small size of the MinION allows for in-house sequencing, while its specific sequencing method allows for multiple samples to be run at once if using barcodes. To perform a sequencing run with the MinION, the MinKNOW software, the flongle flow cell (R9.1), and the flongle flow cell adapter were necessary. Additionally, the 16s Barcoding Kit 1-24 from Oxford Nanopore Technologies was used for the library prep of the DNA. Bioinformatic analysis of the basecalled 16s reads from

MinION was performed using the EPI2ME Desktop Agent software.

To test the consistency and sensitivity of our sequencing protocol, the ZimoBIOMICS Microbial Community DNA Standard was utilized.

Lastly, the martian regolith simulants used were the Mars Global simulant (MGS-1), the Mars Clay ISRU simulant (MGS-1C), and the Mars Sulfate ISRU simulant (MGS-1S) sourced from Exolith Labs.

#### Results and Discussion:

Three preliminary trials utilizing the 16s rapid sequencing kit (SQK-RAD004), Lambda control DNA, and MinION flow cell were conducted. Protocol for the library preparation of the Lambda DNA was sourced from the Rapid Sequencing control experiment kit (SQK-RAD114) with the rest of the protocol using SQK-RAD004. The goal of these tests were simple: get used to the sequencing equipment and understand any issues which may arise in a future run. Additionally, given the experiment is located in Houston, Texas, optimizing for the local environment (higher temperatures and humidity) was important as well.



**Figure 1.** Sequencer setup. Left photo (top down view) is setup used in Trial 1. All following trials used the setup in the right photo (Side on view).

This test was conducted with a flow cell containing 153 pores and was placed in a Styrofoam box with two ice packs (Figure 1). The test was run for 72 hours with the ice packs being changed out once a day. While this test concluded after 72 hours, the number of pores dropped to zero after approximately 24 hours. Additionally, the MinION experienced multiple temperature fluctuations outside of the required temperature range (34 °C) getting as high as 40 °C approximately 48 hours after starting sequencing. Data from this test was not used in further analysis.

The second test utilized a different Styrofoam box setup which allowed for better air circulation, 3 ice packs, and a fan if required. Additionally, a flow cell

with 1511 pores was used and the run was monitored frequently. Unfortunately, the run had to be reset 24 hours in due to a computer restart, thus this run had run for approximately 96 hours (72 hours uninterrupted after the reset). In this test, temperatures tended to dip too low at points (32 °C) after exchanging ice packs. It was determined that there was too much cool air reaching the MinION. Data from this run was not used in further analysis.

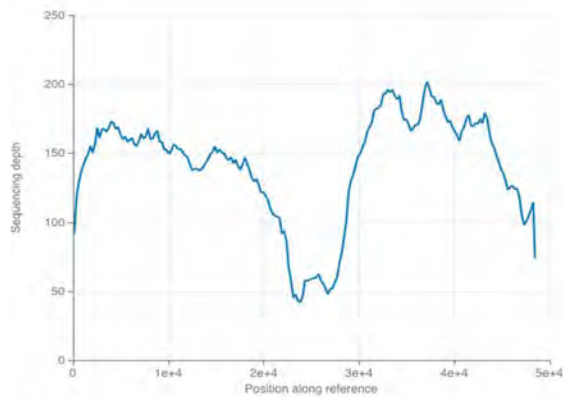


**Figure 2.** coverage of the Lambda DNA reference sequence (J02459.1) with read data from test trial 3. The sequencing depth indicates the number of reads which were aligned to a specific position along the reference sequence.

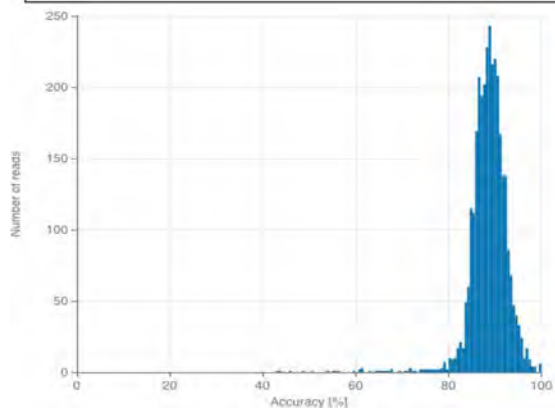


**Figure 3.** alignment accuracy of test trial 3 reads aligned against the Lambda DNA reference sequence (J02459.1).

Test trial 3 utilized the Styrofoam box modifications from the second test. This test ran for 48 hours and only utilized a fan. The flow cell had 307 pores available for this run. In this case, the temperature stayed consistently within the bounds of the ideal range. Furthermore, the basecalled reads were able to be run through multiple workflows within the EPI2ME Desktop Agent and EPI2ME Labs software. The results from the EPI2ME Labs alignment workflow using the Lambda DNA fasta reference sequence are shown in Figure 2 and Figure 3. Out of 3,297 reads, 3,158 reads were able to be aligned

to the Lambda DNA reference sequence (J02459.1) with a mean alignment accuracy of 88.6%.

The Trial 3 results were also run through the EPI2ME Desktop Agent fastq control experiment workflow. This workflow utilizes the Lambda DNA reference sequence (J02459.1) for alignment and works similarly to the alignment workflow in EPI2ME Labs. The analysis yielded very similar results with 3,156 out of 3,279 reads being aligned with a mean alignment accuracy of 88.6%.

The success of the third trial shows that our thermal regulation of the sequencer and the preliminary DNA library preparation protocols have been successful. The next steps is to test our current protocol with the flongle flow cell and the ZymoBIOMICs standard to identify the accuracy and sensitivity of the protocols. Once a repeatable and consistent result is shown using the ZymoBIOMICs and flongle flow cells, the protocol will be suitable for testing with microbial samples from Martian regolith simulants spiked with the ZymoBIOMICs standard. Spiking the simulant will allow us to test our retrieval of DNA and troubleshoot any low species abundances before using the protocol on samples with unknown abundances.

**Conclusion and Future Directions:** Martian habitats will require ISRU practices in order to be sustainable and economically viable [1,2,4]. As such, treatment of Martian regolith will be necessary for crop development. Since chemical processes can be expensive and leave behind toxic products, bioremediation is a promising way to create agriculturally stable soil capable of hosting healthy plants [5,7,8]. Developing a protocol to rapidly sequence 16s rRNA from bioremediating Martian regolith simulants allows for the rapid analysis of these samples. As such, monitoring microbiome changes can provide useful information on what processes are occurring in the regolith samples.

**Acknowledgments:** I would like to thank Dr. Kennda Lynch for mentoring me throughout the summer program. I would also like to thank Jessica Lopez, Dr. Anna Simpson, Dr. Rafael Loureiro, and Delia Enriquez for their help throughout the summer.

#### References:

- [1] Duri L. et al. (2022) *Frontiers in Astronomy & Space Sci.*, 8, 233. [2] Frackrell L.E. et al (2021) *Icarus*, 354, 114055. [3] Wamelink G.W. et al. (2014) *PLoS One*, 9, e103138. [4] Verseux C. et al. (2016). *Internat. J. Astrobio.*, 15, 65-92. [5] Youngblut M.D. et al. (2016) *Annual Review of Microbio.*, 70, 435-457. [6] Poulet L. et al. (2022) *Frontiers in Astronomy & Space Sci.*, 8, 226. [7] Coates J.D. (2004) *Nature reviews. Microbio*, 2, 569-580. [8] Bardiya N. and Bae J.H. (2011) *Microbio. Research*, 166, 237-254. [9] Lynch K.L. et al. (2019) *Astrobiology*, 19, 629-641.

**MORPHOMETRIC CHARACTERIZATION OF LUNAR LANDING SITES.** J. M. McCallion<sup>1,2</sup>, S. J. Lawrence<sup>3</sup>, J. D. Stopar<sup>1</sup>, <sup>1</sup>Lunar and Planetary Institute (USRA), Houston, TX 77058, USA <sup>2</sup>Rowan University, Glassboro, NJ, 08028, USA (mccall72@students.rowan.edu), <sup>3</sup>Astromaterials Research and Exploration Science, Code X13, NASA Lyndon B. Johnson Space Center, Houston, TX, USA

**Introduction:** The NASA Lunar Reconnaissance Orbiter (LRO) has been orbiting the Moon and collecting data about the lunar surface and environment since 2009 [1-3]. NASA has commenced a new program of lunar exploration and development [4]. The prerequisite for useful lunar surface operations is a successful landing, defined here as one where the spacecraft is intact, operational, and capable of conducting its mission. As the Artemis campaign gets underway, it is important to develop standardized methods for assessing candidate landing sites. One way of doing this is to determine morphologic metrics including slope, Terrain Ruggedness Index (TRI), and rock abundance [5,6].

**Objectives:** In this project, we determine the physical parameters of the lunar surface at 16 successful lunar landing sites where Lunar Reconnaissance Orbiter Camera (LROC) observations have been used to create Digital Terrain Models (DTMs) [7]. Our aim is to determine a reference set of parameters built from historical landings that can serve as a guide for the analysis of future candidate sites. While each future landing may have unique requirements and spacecraft, our reference set may provide helpful context in the definition of morphologic requirements for safety. We derive slope and TRI from elevation data [8], and rock abundance from LRO Diviner surface temperature data [9].

Another objective of this project is to determine how the derived morphologic parameters for the same landing site change between common pixel scales. In ideal lighting conditions, 2m/px Narrow Angle Camera Digital Terrain Models (NAC DTMs) can be assembled using LROC stereoscopic imagery from two or more concentric orbits of the LRO [7]. However, due to low light conditions near the lunar poles, the highest quality data for many potential lunar landing sites comes from the Lunar Orbiter Laser Altimeter (LOLA) data, which have been resampled to 5m/px postings in some locations [10]. Therefore, we seek to assess how the derived slope and TRI values change as a function of changes in the DTM postings from 2m/px to 5m/px. The resampled 5m/px NAC DTMs will serve as an analogue for the LOLA elevation data that will be available for mission planning near the lunar south pole. This will enable us to distinguish how far the parameters diverge from the parameters recorded at 2-m pixel scaling, and help quantify whether LOLA, or

5m/px, topographic data are of sufficient pixel scaling for assessing potential landing ellipses.

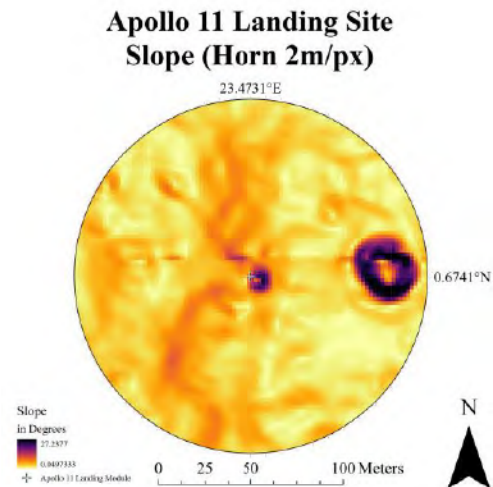


**Figure 1:** Derived slope values of the Apollo 11 Landing Site

**Methods and Data:** We downloaded publicly available LROC DTMs for 16 historic landing locations from NASA's Planetary Data System (PDS) and ingested them for further processing and analysis in the USGS Integrated Software for Imagers and Spectrometers (ISIS) [11]. We note that 12 of the legacy lunar landing sites have 2m/px elevation data, but due to operational changes in the orbital parameters of LRO four of the more recent landing locations have lower native pixel scaling.

We subsequently verified dataset positional accuracy in ArcGIS Pro using high resolution orthophotos of each site to align and record the precise coordinates of the landing module. Using these data, we identified the landing module coordinates. After identification of touchdown location, we used the DTMs to determine morphologic values for a 100m circular radius surrounding the landing module.

Using the Geospatial Data Abstraction Library (GDAL), we generated slope data with the Horn algorithm and TRI data with the Wilson algorithm for each landing site [12]. *Fig. 1* shows the slope data for the Apollo 11 landing site at 2m/px. Each DTM has a corresponding confidence map that indicates pixels that may not have accurate values (*fig. 2*). These maps were used to determine the concentration of low-confidence pixels as a percentage of the total pixels in the sample area near the lander.

We manually registered the Diviner-derived global rock abundance data to identify and extract the relevant rock abundance value for each landing site coordinate. We resampled each 2m/px DTM to 5m/px, generated slope and TRI data using the 5m/px DTMs as the input and recorded the values. To assess the average quantitative discrepancy, we calculated the absolute difference of the mean values between the 2m/px and 5m/px data for slope and TRI. To assess the potential difference between commonly employed methods of calculating slope, we also calculated slope values for the historic landing sites. Each site had additional slope values calculated using the 4-corners algorithm to gauge the quantitative difference between the outputs of the two algorithms at this sample area size, and pixel scaling. Lastly, we resampled the Apollo 11 landing site DTM incrementally between 2m and 45m, generated slope and TRI values for each pixel scaling and plotted the values.

**Results:** The morphometric parameters for the successful lunar landing sites in this analysis are:

- **Slope:**  $\leq \sim 8.39^\circ$  (fig. 3)
- **TRI:**  $\leq \sim 0.57$  m (fig. 4)
- **Rock Abundance:**  $\leq 0.015$  (fig. 5)

The average difference between the 2m/px and 5m/px derived datasets are:

- **Slope:**  $\sim -0.28^\circ$
- **TRI**  $\sim 0.19$  m

The average percentage of low confidence pixels in the cropped landing site DTMs is  $\sim 6.85\%$ , and the difference between the Horn and 4-Corner methods' average slope value is  $\sim 0.03^\circ$ . Resampled from 2m/px to 45m/px, the Apollo 11 landing site average slope decreases by  $\sim 1^\circ$ , and TRI increases by  $\sim 1$ m. These average differences are relatively small and within the inherent uncertainties of the data.

**Discussion:** The results of this analysis improve upon previous results [5,6] and offer a basis for comparison for more recent landed missions [13]. Our analysis demonstrates that as DTM pixel scale decreases from 2 to 45 m, slope values may slightly decrease, and TRI values increase. The margin of observed differences is relatively small between 2m/px and 5m/px, increasing confidence that 5m/px DTMs can be successfully employed when NAC-derived 2m/px models are not available.

The pixel scale of the rock abundance dataset is greater in comparison to the scale that this analysis takes place. At  $\sim 236$  m/px, an entire landing site sample area fits well within a single rock abundance pixel. As such, the rock abundance metric has been recorded as a single value for each site instead of an average from a larger dataset. The average low confidence pixel percentage of  $\sim 6.85\%$  does not mean that 6.85% of the

DTM pixel values are wildly incorrect. Instead, this percentage is representative of the number of pixels that could be off slightly due to various limitations of the DTM production process. Lastly, the average difference between the Horn and 4-corner methods of  $.03^\circ$  at this scale means that the two algorithms are practically interchangeable.

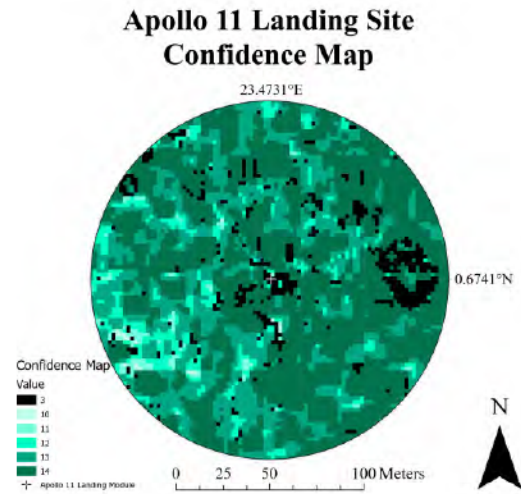


**Figure 2: Apollo 11 Confidence Map**  
(3: Low Confidence, 10-14: High Confidence)

**Conclusions:** The metrics recorded in this analysis provide a new and improved baseline set of data to distinguish discrete locations where a safe landing on the lunar surface can be accomplished.

NAC-derived DTMs with 2-m pixel scales remain the best possible products to use to provide topographic data from potential candidate landing sites. However, these new data also provide increased confidence that newer LOLA data products are adequately capturing the nature of the lunar terrain in situations where NAC DTMs are unavailable. Future mission planners can leverage these outcomes to facilitate lunar exploration activities for both science and exploration purposes.

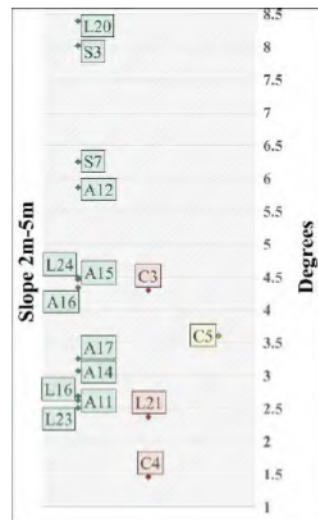
**Acknowledgments & Data Sources:** This work uses NASA LRO data from the PDS. The work was supported by the LPI Intern Program.

**References:** [1] J. W. Keller, N. E. Petro, and R. R. Vondrak, "The Lunar Reconnaissance Orbiter Mission – Six years of science and exploration at the Moon," *Icarus*, vol. 273, pp. 2–24, Jul. 2016, doi: 10.1016/j.icarus.2015.11.024. [2] G. Chin *et al.*, "Lunar Reconnaissance Orbiter Overview: The Instrument Suite and Mission," *Space Sci. Rev.*, vol. 129, no. 4, pp. 391–419, Apr. 2007, doi: 10.1007/s11214-007-9153-y. [3] R. Vondrak, J. Keller, G. Chin, and J. Garvin, "Lunar Reconnaissance Orbiter



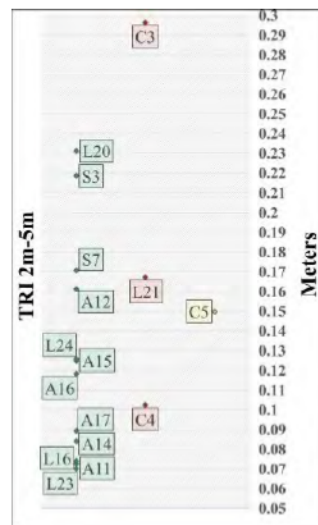
(LRO): Observations for Lunar Exploration and Science,” *Space Sci. Rev.*, vol. 150, no. 1–4, pp. 7–22, Jan. 2010, doi: 10.1007/s11214-010-9631-5. [4] NASA, “A Bold New Era of Human Discovery: Report of the Artemis III Science Definition Team,” United States Government Printing Office, Washington, D. C., NASA Special Publication NASA/SP-20205009602, 2020. [5] S. J. Lawrence, J. D. Stopar, B. L. Jolliff, E. J. Speyerer, and M. S. Robinson, “Lunar Surface Traverse and Exploration Planning: What Makes a ‘Good’ Landing Site?,” in *Annual Meeting of the Lunar Exploration Analysis Group*, Columbia, MD, USA: Lunar and Planetary Institute, 2015, p. 2074. [6] S. J. Lawrence *et al.*, “Morphologic Parameters for Successful Lunar Landing Sites,” Lunar and Planetary Science Conference 51, Abstract, 2579, Mar. 2020, The Woodlands, TX. [7] M. R. Henriksen, M. R. Manheim, E. J. Speyerer, M. S. Robinson, and L. Team, “Extracting accurate and precise topography from LROC narrow angle camera stereo observations,” *Int. Arch. Photogramm. Remote Sens. Spat. Inf. Sci.*, vol. 41, p. 397, 2016. [8] M. F. J. Wilson, B. O’Connell, C. Brown, J. C. Guinan, and A. J. Grehan, “Multiscale Terrain Analysis of Multibeam Bathymetry Data for Habitat Mapping on the Continental Slope,” *Mar. Geod.*, vol. 30, no. 1–2, pp. 3–35, 2007, doi: 10.1080/01490410701295962. [9] J. L. Bandfield, R. R. Ghent, A. R. Vasavada, D. A. Paige, S. J. Lawrence, and M. S. Robinson, “Lunar surface rock abundance and regolith fines temperatures derived from LRO Diviner Radiometer data,” *J. Geophys. Res. Planets*, vol. 116, no. E12, p. n/a-n/a, 2011, doi: 10.1029/2011JE003866. [10] M. K. Barker, E. Mazarico, G. A. Neumann, D. E. Smith, M. T. Zuber, and J. W. Head, “Improved LOLA elevation maps for south pole landing sites: Error estimates and their impact on illumination conditions,” *Planet. Space Sci.*, vol. 203, p. 105119, Sep. 2021, doi: 10.1016/j.pss.2020.105119. [11] L. Keszthelyi *et al.*, “Utilizing the Integrated Software for Imagers and Spectrometers (ISIS) to Support Future Missions,” presented at the Lunar and Planetary Science Conference, Mar. 2014, p. 1686. Accessed: Jun. 26, 2015. [12] GDAL/OGR contributors, *GDAL/OGR Geospatial Data Abstraction software Library*. Open Source Geospatial Foundation, 2023. doi:10.5281/zenodo.5884351. [13] R. N. Clegg Watkins *et al.*, “Photometric characterization of the Chang’e-3 landing site using LROC NAC images,” *Icarus*, vol. 273, pp. 84–95, Jul. 2016, doi: 10.1016/j.icarus.2015.12.010.

Figure 3: Slope Plot (2-5m)



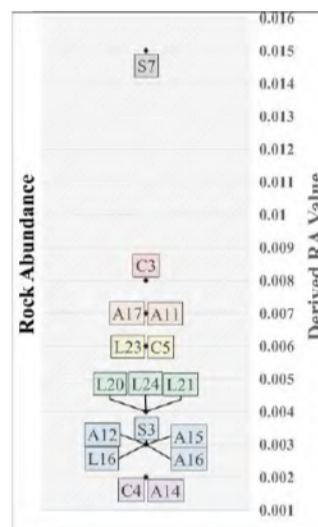
**Figure 3-5:**  
A- Apollo  
L- Luna  
S- Surveyor  
C- Chang’e

Figure 4: TRI Plot (2-5m)



**Figure 3-4:**  
2m/px  
5m/px  
3m/px

Figure 5: Rock Abundance Plot





**Analysis of the Surface Albedo at Jezero Crater as Determined from the Meteorological Station on board NASA's Mars 2020 Mission.** P. Raghav<sup>1</sup> and G.M. Martínez<sup>2</sup>, <sup>1</sup>Electrical Engineering, Aligarh Muslim University, Aligarh 202002, <sup>2</sup>Lunar and Planetary Institute, 3600 Bay Area Blvd. Houston TX.

**Introduction:** Albedo is the fraction of solar incoming radiation that is reflected from a surface. It is a key factor in understanding Mars' surface and climate because it affects how much solar energy is absorbed or reflected, influencing surface temperatures, ice stability, and weather patterns [1]. Thus, studying albedo is important for exploring water resources and climate conditions in preparation for future human exploration. The main goal of this study is to analyze albedo values measured by the Mars Environmental Dynamics Analyzer (MEDA, [2]) on board NASA's Mars 2020 mission for the first 684 sols of the mission. This work complements and extends a previous study covering the first 350 sols [3].

**Data:** MEDA is one of the seven science instruments on board the Perseverance rover. Designed to measure weather conditions across Perseverance's traverse, MEDA consists of five sensors. This abstract focuses on two of these: the Thermal Infrared Sensor (TIRS) and the Radiation and Dust Sensor (RDS). TIRS, an infrared radiometer, utilizes five channels in different wavelengths to measure various parameters [3]. IR3 is one of these channels and it measures reflected (upwelling) solar flux in the 0.3-3  $\mu\text{m}$  range. Out of RDS's 16 photodiodes, we employ measurements from the panchromatic channel (TOP 7), which measures the downwelling solar flux in the 0.19–1.2  $\mu\text{m}$  range with a hemispherical field of view (FoV) of  $\pm 90^\circ$ . Fig. 1 shows the location of TIRS and RDS on the rover, as well as TIRS' FoV for which the albedo is obtained.

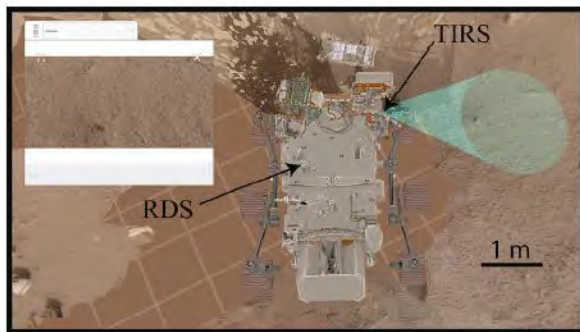


**Figure 1.** FoV (green shaded area) of TIRS/IR3, covering an ellipsoidal area of  $\sim 3\text{-}4\text{ m}^2$ . TIRS is placed on the remote sensing mast  $75^\circ$  clockwise from the rover's forward direction. A zoomed in view of the TIRS' FoV is shown in the top left insert.

**Methodology:** After conversion of RDS/TOP7 measurements to 0.3-3  $\mu\text{m}$  using a radiative model [3], we obtain the broadband hemispherical albedo in the 0.3-3  $\mu\text{m}$  band using TIRS/IR3 and RDS/TOP7 measurements. Within TIRS and RDS datasets, we only considered values when the rover was parked. In addition, we removed RDS values showing saturation at sunrise and noon. Sunrise saturation occurred when the RDS was operating in high gain mode, while noon saturation occurred in the vicinity of noon between sols  $\sim 270$  and 350 when the incident solar flux was higher than the upper bound of the range established in preflight calibrations on Earth [3]. Moreover, we discarded measurements affected by shadows cast by the remote sensing mast on the RDS.

Using the curated dataset, we calculated the phase angle to assess albedo as a function of illumination and viewing geometry. The phase angle ( $\beta$ ) is defined as:

$$\cos \beta = \cos(SZA)\cos(e) + \sin(SZA)\sin(e)\cos(\Delta\phi) \quad (1),$$

where  $\beta$  represents the angle between the incident sunlight, the observer's line of sight, and the normal to the surface at the point of interest, SZA is the solar zenith angle,  $e = 55^\circ$  is the emission angle given the  $-35^\circ$  pointing angle of TIRS/IR3 (Fig. 1), and  $\Delta\phi = |\phi_s - \phi_{TIRS}| + 180^\circ$  is the difference between the solar azimuth angle,  $\phi_s$ , and the TIRS' azimuth angle,  $\phi_{TIRS}$ , which is calculated using rover's yaw,  $\phi_R$ , as  $\phi_{TIRS} = -\phi_R - 75^\circ$ .

**Results:** Fig. 2 (top left), shows the curated collection of MEDA-derived broadband albedo values as a function of local mean solar time (LMST) and solar longitude ( $L_s$ , color bar) for the first 684 sols of the mission. We only included values with SZA  $< 60^\circ$  to mitigate uncertainties near sunrise and sunset. The albedo exhibited a distinct non-Lambertian pattern on each sol, with lower values around noon and higher values towards sunrise and sunset. Note that based on uncertainties in measured solar fluxes, the relative error in albedo is  $< 10\%$  near noon, and  $< 20\%$  towards sunset and sunrise [3]. Fig. 2 (bottom left) shows the daily minimum albedo at noon, with values ranging from 0.10 on sol 184 ( $L_s \sim 90^\circ$ ) to 0.24 on sol 489 ( $L_s \sim 260^\circ$ ).

The right panel in Fig. 2 shows the terrain in these two sols. To assess the non-lambertian behavior

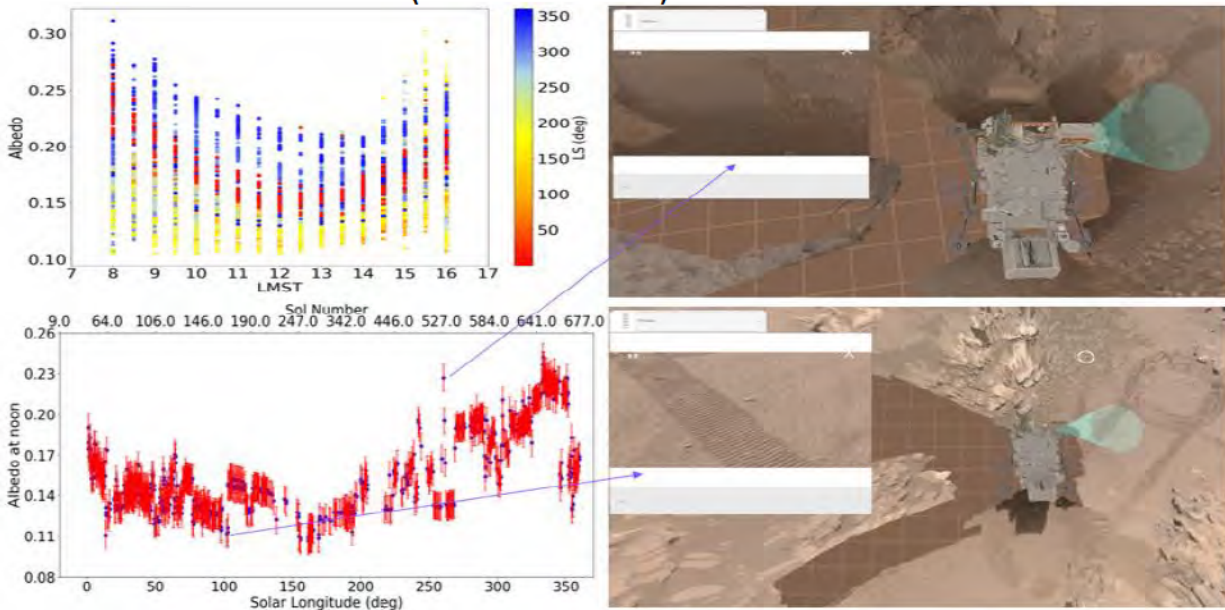


**Figure 2.** (Top left) Variation of broadband (0.3–3  $\mu\text{m}$ ) albedo as a function of LMST and Ls for 684 sols of the mission. (Bottom left) Daily minimum (near-noon)  $\alpha$  as a function of Ls for the first 684 sols of the mission. Images of terrain for maximum (top right) and minimum (bottom right) daily minimum albedo at noon.

of the terrain, we calculated the diurnal relative variation of albedo as:  $|(\alpha_{max} - \alpha_{min})/\alpha_{min}|$ , where  $\alpha_{max}$  and  $\alpha_{min}$  are the minimum albedo values. Fig. 3 (left) shows the diurnal relative variation of albedo over group of sols when the rover was parked.

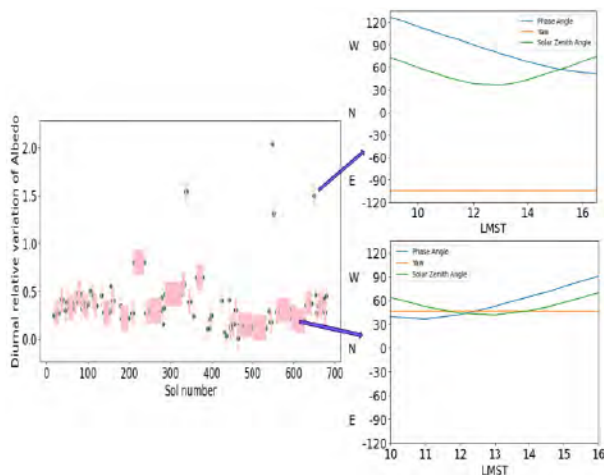


**Figure 3:** (Left) Diurnal relative variation of albedo for first 684 sols on Mars. (Right) Phase angle, rover's yaw, solar zenith angle as a function of LMST (representing viewing geometry) for maximum (top) and minimum (bottom) relative variation in albedo.

Fig. 3 (top right) shows phase angle, rover's yaw, and solar zenith angle as functions of LMST for sol 649, which shows the second largest diurnal relative variation (we excluded the data from sol 549 due to incomplete diurnal coverage). Fig. 3 (bottom right)

presents the same variables for sols 610–627, representing a period with one of the smallest relative variation in albedo (we excluded sols with lower variation due to incomplete diurnal coverage). The rover's yaw angle ( $\phi_R \sim -100^\circ$ ) with the TIRS facing towards the East resulted in the highest relative variation in albedo. On the other hand, the minimum relative variation in albedo was observed when the rover's yaw angle ( $\phi_R \sim 45^\circ$ ) positioned the TIRS facing towards the Northwest, causing the least variation in albedo.

**Conclusions:** On each sol, the albedo exhibited a noticeable non-Lambertian behavior, with the lowest values observed near noon and the highest values towards sunrise and sunset. The minimum daily albedo obtained from MEDA varied between 0.10 and 0.24, depending on the terrain type. The relative variation in albedo varied between 0.190 and 1.495 depending on the viewing geometry. Future research will further analyze the albedo as a function of viewing geometry and will explore the relation between albedo and thermal inertia over an extended period of 684 sols on Mars.

**Acknowledgements:** All the Mars 2020 MEDA data necessary to reproduce each figure shown in this manuscript are available via the Planetary Data System (PDS) Atmospheres node [4].

**References:** [1] Fenton et al. (2007) *Nature*, 446(7136), 646–649. [2] Rodríguez-Manfredi, J. A. et al. (2021) *Spa. Sci. Rev.* 217(3), 1–86. [3] Martínez et al. (2023) *JGR:Planets*, 128, e2022JE007537. [4] Rodríguez-Manfredi, J. A. and Torre Juárez, M. (2021) *PDS Atmospheres Node*, 10, 1522849.

**TESTING HYPOTHESES FOR THE ORIGIN OF MARTIAN ALKALI BASALTS THROUGH FRACTIONAL CRYSTALLIZATION OF PRIMARY MAGMAS.** M. C. Rudin<sup>1,2</sup> and J. B. Balta<sup>1</sup>, <sup>1</sup>The Lunar and Planetary Institute, USRA, 3600 Bay Area Blvd., Houston, TX 77058; <sup>2</sup>Department of Geosciences, University of Texas at Dallas, Richardson, TX 75080 (mia.rudin@utdallas.edu).

**Introduction:** Martian alkali basalts found at Gusev Crater have been proposed to source from a single magma series linked by fractional crystallization [1,2,3]. It was similarly proposed that basalts with still higher alkali enrichment at Gale Crater, such as Jake\_M [4], could also be part of a similar magma series, except formed under different crystallization conditions [5,3]. If the alkali basalts at Gale and Gusev Crater both represent a single magma series, this could indicate simple and global magmatic processes and compositions exist on Mars. If this hypothesis is not supported, it would suggest that the formation of these alkali basalts requires distinct melting processes at each site. Context for the formation of the alkali basalts at Gale Crater will therefore benefit the overall understanding of Martian volcanism.

The MELTS family of algorithms [6,7,8,9,10] are the set of thermodynamic modeling tools most often used to simulate Martian igneous systems. MELTS algorithms use Gibbs free energy minimization to calculate stable phase equilibria and are capable of computing automated fractional and equilibrium crystallization paths [11]. The THERMOCALC suite of algorithms [12,13,14,15,16,17] is another set of common modeling tools that, in general, solve a series of non-linear equations to produce a phase diagram [11], a process that requires hours to produce results. However, a newly published software package, MAGEMin [18], or Mineral Assemblage Gibbs Energy Minimizer, produces point-wise results based on the THERMOCALC database in seconds.

Hernández-Urbe et al. (2022) [11], Otto et al. (2023) [19], and Astudillo Manosalva [20] each conducted a series of calculations using MELTS and THERMOCALC, finding that the tools have distinct compositional ranges where their calculations are more accurate. These studies indicate that THERMOCALC algorithms, such as MAGEMin, may be calibrated to model the formation of alkali basalts, such as those on the Martian surface, more accurately. However, this has not been previously done.

We conducted a series of fractional crystallization calculations in MAGEMin to test the hypothesis that alkali basalts at Gale Crater are related to Gusev near-primary magmas by fractional crystallization, and then compared results to those previously calculated in MELTS to assess their differences. If MAGEMin results do not support the hypothesis, this would indicate that Gale alkali basalts were formed from distinct melting processes or a metasomatized source.

**Methodology:** We use the same measured Martian near-primary magma compositions Humphrey [21,1,3] and Fastball [22,3], temperatures, and pressures from MELTS calculations by Udry et al. (2014) and McSween et al. (2006) (Table 1) to compare their results to ours done using MAGEMin.

A MAGEMin interface in the Julia programming language allows us to calculate single point-wise compositions. To calculate a fractional crystallization path, we input a measured near-primary composition, temperature, and pressure from literature (Table 1) to produce an output. We record the result composition, then reenter it with a 10°C-temperature drop in sequence. This process is repeated to produce a series of points, making up an isobaric fractional crystallization path comparable to the results of Udry et al (2014) and McSween et al. (2006). MAGEMin calculations are unautomated and not user-friendly for fractional crystallization. Conducting a single calculation requires the user to manually input and record results at each step. We conducted over 500 calculations, producing 17 isobaric fractional crystallization paths (Table 1) that bracket results of previous studies using the MELTS algorithm to test the hypothesis.

Primary Magma	Pressure	Water Content
Fastball	1, 6, 12 kbar	0 wt.%
Humphrey	1, 6, 12 kbar	0 wt.%
Fastball	1, 6, 12, 14 kbar	0.5 wt.%
Humphrey	1, 10 kbar	0.5 wt.%
Fastball	1, 6, 12 kbar	1.67 wt.%
Fastball (FMQ-3)	1, 12 kbar	0.5 wt.%

**Table 1.** Input parameters chosen from Udry et al. (2014) and McSween et al. (2006) for the 17 isobaric fractional crystallization path calculations done in MAGEMin.

**Results:** Using MAGEMin, the highest alkali contents produced from fractional crystallization of a Fastball-like primary magma occurred at the highest H<sub>2</sub>O content and pressure (1.67 wt.% H<sub>2</sub>O, 12 kbar), reaching over 6 wt.% total alkali content. The highest alkali content from a Humphrey-like primary magma, similarly, was produced under the highest pressure and H<sub>2</sub>O contents calculated (0.5 wt.% H<sub>2</sub>O, 10 kbar).

In all calculations, Na<sub>2</sub>O/K<sub>2</sub>O ratios drop with increased crystallization, but drop sooner at higher

pressure conditions and lower H<sub>2</sub>O contents. The fractional crystallization of a dry Fastball composition at 1 kbar yields the most potassic ratio of those tested.

We recalculated the Fastball composition at an F<sub>O</sub><sub>2</sub> of FMQ-3 for an additional set of calculations [23] (Table 1), resulting in significantly increased total alkali content at both 1 and 12 kbar (Fig. 1). The Na<sub>2</sub>O/K<sub>2</sub>O ratios of a reduced composition decrease sooner than calculations with oxidized starting compositions.

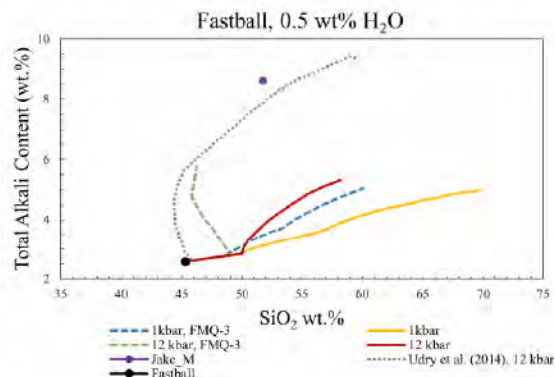


**Figure 1.** 4 fractional crystallization paths of reduced and oxidized Fastball compositions with 0.5 wt.% water at 1 and 12 kbar.

**Discussion:** Using MELTS, McSween et al. (2006) suggested that the Gusev alkali basalts represent a magma series linked through fractional crystallization, and our MAGEMin results support those findings.

Jake\_M, an alkali basalt found at Gale Crater, has particularly high alkali content (8.62 wt.%), and a Na<sub>2</sub>O/K<sub>2</sub>O ratio of 2.86. Udry et al. (2014) finds that a Fastball composition with 0.5 wt.% H<sub>2</sub>O at 12 kbar fractionally crystallizes to a Jake\_M-like total alkali composition using MELTS (Fig. 1). In MAGEMin, adding H<sub>2</sub>O into the starting composition yields elevated total alkalis with increasing pressure, but our results have still significantly lower alkali contents compared to MELTS at the same conditions, and none reach an alkali content like Jake\_M (Fig. 1).

Low Na<sub>2</sub>O/K<sub>2</sub>O ratios are supported by low water contents. The closest ratio to Jake\_M of all tested, approximately 5.17, was produced from a Fastball composition with no H<sub>2</sub>O at 1 kbar. This difference may be explained by the rate plagioclase crystallizes; if H<sub>2</sub>O content is high, plagioclase crystallization is suppressed and less Na is removed from the melt, which results in lower alkali contents.

MAGEMin results suggest that liquid lines of descent are defined by whether olivine or pyroxene crystallizes first. At 1 kbar, MAGEMin tends to crystallize olivine before pyroxene, whereas in MELTS results, unless the composition includes high H<sub>2</sub>O

contents (1.67 wt.%), orthopyroxene crystallizes before olivine. If pyroxene crystallizes first, SiO<sub>2</sub> is depleted sooner, and alkali contents are elevated at a given SiO<sub>2</sub> content (Fig. 1). This effect is magnified in the reduced case, where there is additional divalent iron. However, this is contrary to findings in Udry et al. (2014), that F<sub>O</sub><sub>2</sub> does not significantly impact liquid lines of descent.

Because alkali basalts may more closely match experiments used to calibrate THERMOCALC databases, results calculated in MAGEMin may be more accurate than results previously done in MELTS. Our results do not support hypotheses that alkali basalts at Gale Crater are related to Gusev primary magmas by fractional crystallization, and instead suggest a distinct melting process at each site or a metasomatized source for Gale alkali basalts.

**Acknowledgments:** This work was supported by the 2023 LPI's Summer Internship Program in Planetary Science and a Cooperative Agreement between NASA's Science Mission Directorate and the LPI, operated by the USRA.

**References:** [1] McSween, H. Y. et al. (2006) *J. Geophys. Res.*, 111. [2] Tuff, J. et al. (2013) *Nature*, 498, 342–345. [3] Udry, A. et al. (2014) *J. Geophys. Res. Planets*, 119, 1–18. [4] Grotzinger, J. P., et al. (2013) *Lunar Planet. Sci. XLIV*, Abstract 1259. [5] Stolper, E. M., et al. (2013) *Sci.*, 341. [6] Ghiorso, M. S. and Sack, R. O. (1995) *Cont. to Min. and Petr.*, 119(2), 197–212. [7] Ghiorso, M. S. et al. (2002) *Geochem. Geophys. Geosyst.*, 3(5). [8] Asimow, P. D. et al. (2004) *G. G. G.*, 5. [9] Smith, P. M. and Asimow, P. D. (2005) *G., G., G.*, 6, Q02004. [10] Gualda, G. A. R. et al. (2012) *Journ. of Petr.*, 53(5), 875–890. [11] Hernández-Urbe, D. et al. (2022) *Am. Min.*, 107(9), 1789–1806. [12] Holland, T. and Powell, R. (2003) *Cont. to Min. and Petr.*, 145(4), 492–501. [13] Holland, T. J. B. and Powell, R. (2011) *Journ. of Meta. Geo.*, 29(3), 333–383. [14] Holland, T. J. B. et al. (2013) *Journ. of Petr.*, 54(9), 1901–1920. [15] Holland, T. J. B. et al. (2018) *Journ. of Petr.*, 59(5), 881–900. [16] Powell, R. et al. (1998) *Journ. of Meta. Geo.*, 16(4), 577–588. [17] Powell, R. and Holland, T. (2010) *Elem.*, 6(5), 309–314. [18] Riel, N. et al. (2022) *G., G., G.*, 23. [19] Otto, T. S. et al. (2023) *Lithos*, 444–445, 107111. [20] Astudillo Manosalva (Personal communication, 2023) [21] Monders, A. G., E. et al. (2007), *Meteorit. Planet. Sci.*, 42, 131–148. [22] Filiberto, J., et al. (2010), *Geophys. Res. Lett.*, 37, L13201. [23] Kress, V. C. and Carmichael, I. S. E. (1991) *Cont. to Min. and Petr.*, 108: 82–92.

**TOPOGRAPHIC CHARACTERIZATION AND EVOLUTIONARY MODELING OF LARGE VOLCANO-TECTONIC STRUCTURES ON VENUS.** Alexa Schultz<sup>1,2</sup> and Patrick McGovern<sup>1</sup>, <sup>1</sup>Lunar and Planetary Institute (USRA), Houston, TX 77058, <sup>2</sup>Yale University Department of Earth and Planetary Sciences, New Haven, CT 06510.

**Introduction:** The surface of Venus is dominated by volcanic features; there are over 80,000 volcanoes on Venus as detected by radar imaging from the Magellan mission in the early 1990s [1]. One of these volcanic landforms, the corona, is defined by the International Astronomical Union simply as an “ovoid-shaped feature” [2]. This term has taken on new meaning since its original definition, and now the general assumption amongst many planetary scientists is that all coronae formed via the upwelling of hot mantle material.

Here, we take a quantitative approach to characterizing the topographic natures of large volcano-tectonic structures on Venus, applying the Hankel transform method. We apply these results to find affinities and differences between structures and to evaluate the utility of existing classification schemes. We also calculate quantitative models of evolving volcanic edifice topography, in order to evaluate the conditions that contribute to producing the wide range of shapes of volcano-tectonic structures on Venus.

**Methods:**

*Data analysis.* The base Venus topography dataset is the Global Topographic Data Record GTDR-SINUS.3;2 [3]. We determine the topographic signatures of specific volcano-tectonic constructs on Venus, spanning the classifications “Mons” and “Corona” [4, 5], using the pyGMT mapping package [6]. We collect topographic cross-sections along 24 distinct azimuths (15° intervals) and at a 5 km spacing out to 450 km. These are averaged to create a mean topographic profile.

We use the Hankel transform, the axisymmetric analog of Fourier series, to analyze the topographic signatures of large volcanic constructs on Venus, following [7]. An axisymmetric function  $h(r)$  (such as the mean topographic profiles described above) can be expressed as a function of wavenumber  $k$  by a zeroth-order Hankel transform:

$$h(k) = \int_0^{\infty} h(r) J_0(k r) r dr \quad (1)$$

where  $J_0$  is the zeroth-order Bessel function of the first kind. The inverse Hankel transform returns  $h(r)$  in the spatial domain:

$$h(r) = \int_0^{\infty} h(k) J_0(k r) k dk \quad (2)$$

In practice, we use a trapezoidal integration scheme [e.g., 7] to integrate the forward and inverse Hankel transforms, for example, representing a function via a sum of power spectrum coefficients  $h_n$  multiplied by scaled zeroth-order Bessel functions:

$$h(r) = \sum_{n=1}^{nk} h_n J_0(k_n r) \quad (3)$$

To determine the  $k_n$ , quantities  $dy = 0.2$  and  $nk = 360$  set the spacing in wavenumber space and number of wavenumbers, respectively. A variable  $y$  ranges from  $dy/2$  to  $(nk-1/2) * dy$  in increments of  $dy$ , and  $k_n = y_n/r_0$ , where  $r_0$  is a scaling radius (for the topographic analysis, we set  $r_0 = 500$  km). The  $h_n$  coefficients are determined by trapezoidally integrating equation 1.

We obtain the following quantities from the topographic power spectra of Venus volcanic structures: the wavelength ( $\lambda_L$ ) and power ( $P_L$ ), the wavelength ( $\lambda_{max}$ ) and power ( $P_{max}$ ) at the maximum topographic power peak, the wavelength ( $\lambda_{min}$ ) and power ( $P_{min}$ ) at the minimum topographic power peak, and the wavelength ( $\lambda_A$ ) and power ( $A_{max}$ ) at the absolute maximum topographic power peak. We then define four non-dimensional parameters [e.g., 8] defining several aspects of the volcanic topography.

$$\Pi_1 = A_{max}/P_L \quad (4)$$

$$\Pi_2 = |P_{min}/P_L| \quad (5)$$

$$\Pi_3 = \lambda_A/\lambda_L \quad (6)$$

$$\Pi_4 = \lambda_{min}/\lambda_L \quad (7)$$

$\Pi_1$  describes edifice nature,  $\Pi_2$  describes annular nature,  $\Pi_3$  describes the dominant spectral peak nature, and  $\Pi_4$  describes the importance of a short wavelength minimum.

*Modeling.* We model self-consistent growth of a volcanic edifice on Venus by calculating the interaction of the lithospheric stress state generated by lithospheric flexure with favored magma ascent pathways [9, 10, 11]. The stress state in a lithosphere with elastic thickness ( $T_e$ ) is calculated for a given load using the method of [7], using the integration scheme described above to determine a load function  $q(r) = \rho g h(r)$ , where  $\rho = 2800$  kg/m<sup>3</sup> is the density of basalt and  $g = 8.87$  m/s<sup>2</sup> is the surface gravity of Venus. The load distribution is modeled iteratively – in each model, a characteristic magma source radius ( $r_0$ ), central height ( $h_0$ ), and shape (cone, truncated cone, or annulus) are defined [11]. Magma distribution is then subdivided into a number,  $n_{inc}$ , of equal height increments. We use  $n_{inc} = 1, 5, 10$ , or 20; a low  $n_{inc}$  value corresponds to a high magma flux rate relative to the characteristic response time of the flexing lithosphere, and vice versa [11]. For a given stress state, magma ascent at a given location depends on two criteria [9, 10]: favorable horizontal normal stress orientations (horizontal extension [12]) and gradients (extension increasing upward [13]). Our model evaluates these criteria as functions of radius  $r$  at a discrete set of points, with allowances for favorable stress (e.g., regional) and stress gradient (e.g., magma buoyancy) terms that offset adverse values. Then the

magma height for the current increment is assigned to points in  $r$  where both ascent criteria are satisfied; at points where one or both criteria are violated, the magma is diverted to the closest value of  $r$  where both ascent criteria are satisfied. Then the material is distributed according to an algorithm [14] simulating lateral motion of flowing lava that enforces downward flow over pre-existing topography and conservation of mass. Then a new flexural stress state is calculated for a load comprising the load from previous increments plus the just-calculated load distribution for the new increment, and the cycle is repeated up to  $n_{inc}$  times. The resulting model topographic profiles can be characterized via the same techniques described above for the topographic profiles of actual Venus volcano-tectonic constructs.

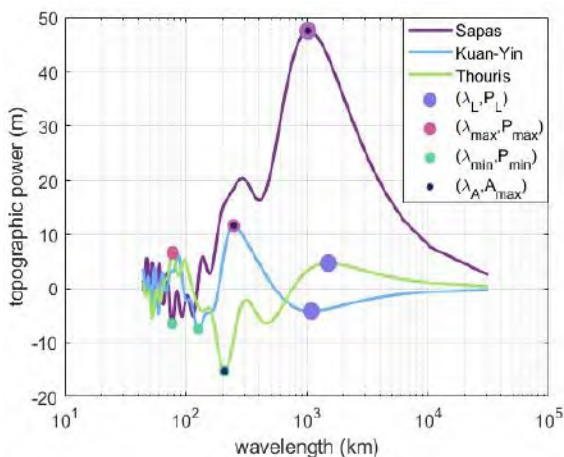


**Figure 1.** Hankel transform topographic power spectra [7] of three volcanic structures on Venus with the longest wavelength peak plotted as a purple dot, maximum topographic power peak plotted as a pink dot, minimum topographic power peak plotted as a teal dot, and absolute maximum topographic power peak plotted as a navy dot. Sapas Mons (purple line) is a conical volcano, Kuan-Yin Corona (blue line) is an annular volcanic construct, and Thouris Corona (green line) is a hole-like structure.

**Results and Discussion:** We analyzed the topographic signatures of 49 volcano-tectonic features on Venus; results for three characteristic shapes are shown in Figure 1. Sapas Mons reflects a conical edifice with a very strong topographic power peak of about 48 m at 1000 km wavelength. The power spectrum declines rapidly as wavelength decreases. For Kuan-Yin Corona, an annular structure, the longest wavelength peak has negative topographic power, and the highest magnitude

peak occurs at a shorter wavelength and lower topographic power than that of Sapas Mons. Thouris Corona represents a class of feature with a deep central depression (“hole”) and minimal surrounding topography. Thouris Corona has a maximum absolute magnitude topographic power negative in sign (opposite to Sapas and Kuan-Yin) and at a short wavelength (similar to Kuan-Yin but opposite to Sapas).

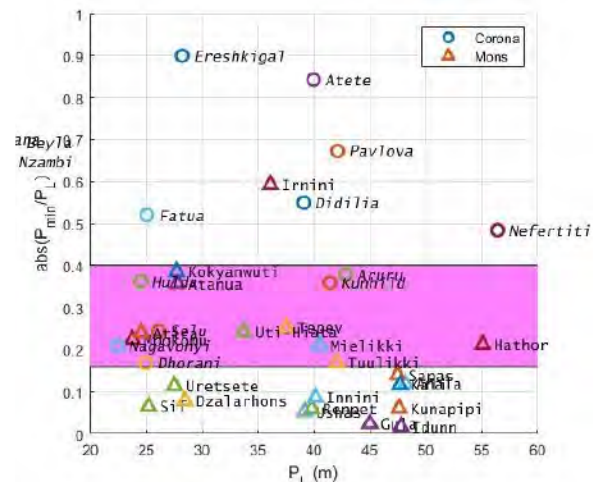


**Figure 2.** Non-dimensional parameter  $\Pi_2$  versus topographic power at longest wavelength peak ( $P_L$ ) for volcanic features classified as corona (circles) and mons (triangles). Pink bar denotes range of  $\Pi_2$  values transitional between mons-dominated (low) and corona-dominated (high) values.

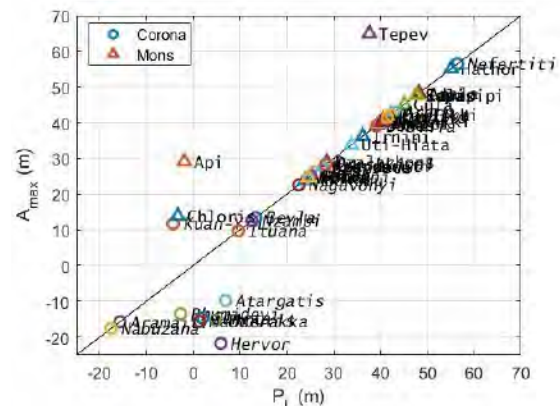


**Figure 3.** Absolute maximum topographic power ( $A_{max}$ , m) versus topographic power at the longest wavelength peak ( $P_L$ , m) for 48 volcanic structures in the classes corona and mons. 39 plot on the one-to-one line and 33 plot above the (20,20) location. A cluster of 5 coronae with deep central lows (“holes”) occur below the one-to-one line. Nyx Mons, at (104,104), is not pictured.



We use the topographic power spectra information to characterize the topography of large volcano-tectonic constructs on Venus. For example, examination of the  $\Pi_2$  parameter (Figure 2) demonstrates three characteristic groupings: features with classifications mons and corona both appear in a band  $0.16 < \Pi_2 < 0.4$ . For lower values, features designated montes dominate, whereas for higher values, features designated coronae dominated. Exceptions to this trend include features with a strong annular topographic signature such as Irimini Mons, which may have been classified as a mons due to complications related to the naming of the feature Sappho Patera at the same location.

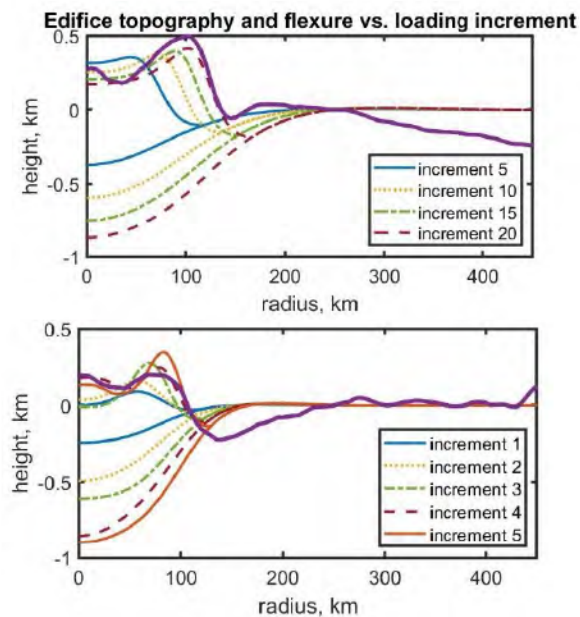


**Figure 4** Average topography (purple line) of 24 radial profiles equally spaced in azimuth of two volcanic structures on Venus, with surface topography and lithosphere surface flexure for several increments in a self-consistent model of lithosphere-directed magma ascent in volcanic construction [x]. **(a, top)** Topography of Fatua Corona with 4 given increments of a 20-increment model ( $T_e = 35$  km,  $r_0 = 75$  km,  $h_0 = 6$  km, annular source). **(b, bottom)** Topography of Kuan-Yin Corona with 5 given increments of a 5-increment model ( $T_e = 15$  km,  $r_0 = 100$  km,  $h_0 = 2$  km, annular source).

A visualization of the components of the  $\Pi_1$  parameter (Figure 3) reveals a “main sequence” along the 1:1 line containing 39 features; for power values greater than 20 m, 33 features classified mons and corona are intermixed with no discernable pattern. We suggest that such structures could be volcanic edifices

dominantly constructed by surface flows, even those that have been given the classification “corona”. These latter could be considered “strangely shaped volcanic edifices” [9]. Features with a deep central depression (“holes”) plot below the 1:1 line in the bottom left. These 6 structures are all classified as coronae, but we suggest that they are likely to have a different formation mechanism than coronae that lie on the 1:1 line.

Our models of volcanic edifice construction allow us to evaluate scenarios for the evolution of volcano-tectonic structures. For example, Kuan-Yin Corona has an average profile with a central high, annular low, and outer annular rim. This morphology is replicated in the last two increments of the model shown in Figure 4b. Note that the initial increments of this model do not have the central high, indicating that a given volcanic edifice may exhibit different topographic profiles at different points in its growth. The average profile of Fatua Corona exhibits a stronger outer annular peak and weaker central high than Kuan-Yin. Fatua’s morphology is replicated in the final increment of the model in Figure 4a. The early shape of the model edifice is much more domical than that of the final increment, demonstrating that volcanic construction models for coronae can produce evolving edifice shapes.

**Acknowledgments:** This work was supported by the LPI’s Summer Intern Program and LPI’s cooperative agreement. We acknowledge Rob Comer for his contributions to establishing the Hankel transform techniques used in this work.

**References:** [1] Hahn, R. M., & Byrne, P. K. (2023). *JGR: Planets*, 128, e2023JE007753. [2] International Astronomical Union (2018) <https://planetarynames.wr.usgs.gov/>. [3] USGS Astropedia Lunar and Planetary Cartographic Catalog <https://astrogeology.usgs.gov/search?pmi-target=venus> [4] E. R. Stofan et al. (1997) in *Venus II*, U. of Arizona Press, 931-965. [5] L. S. Crumpler et al. (1997) in *Venus II*, U. of Arizona Press, 697-756. [6] L. Uieda et al. (2023) <https://zenodo.org/record/7772533> [7] Comer (1983). *Geophys. J. R. astr. Soc.*, 72, 101–113. [8] Merle O. & Borgia A. (1996), *JGR*, 101, 13805–13817 [9] McGovern P. J. et al. (2013) *JGR: Planets*, 118, 2423–2437. [10] Buz J. and McGovern P. J. (2010) *Lunar and Planetary Science Conference 2010*, abs. 1482. [11] McGovern P. J. and Buz J. (2019) *Lunar and Planetary Science Conference 2019*, abs. 2805. [12] E. M. Anderson (1936) *Proc. R. Soc. Edinburgh*, 56, 128 [13] A. M. Rubin (1995) *Annu. Rev. Earth Planet. Sci.*, 23, 287. [14] Webb H. F. and Jordan T. H. (2001) *JGR: Solid Earth*, 106, 30451–30473.



**The Formation of Sulfate and Carbonate Evaporites in CO<sub>2</sub> rich and CO<sub>2</sub> poor environments.** M. E. Walters<sup>1,2</sup>, T. S. Peretyazhko<sup>3</sup>, S. J. Ralston<sup>3</sup>, B. Sutter<sup>3</sup>, P. D. Casbeer<sup>3</sup>, <sup>1</sup>Lunar and Planetary Institute (USRA), Houston, TX 77058, <sup>2</sup>Tufts University, Medford, MA 02155 (madeline.walters@tufts.edu), <sup>3</sup>Jacobs, NASA Johnson Space Center, Houston, TX 77058

**Introduction:** The diverse mineralogy of Mars can reveal past aqueous processes and climate condition that existed on the planet. Regolith exposed to various aquatic environments could undergo a variety of chemical processes resulting in mineralogical assemblages observed on the present-day Mars. Various missions to Mars revealed an abundance of magnesium and calcium sulfate minerals in the Martian soil [1,2,3,4]. However, the exact conditions under which these minerals formed are still poorly constrained.

Formation of sulfates could have been affected by the presence of dissolved carbonates as Mars's atmosphere was mostly carbon dioxide. The dissolved carbonate could interfere with the sulfate formation as carbonate can also form minerals with magnesium and calcium ions.

The objective of this study were (1) to identify which minerals form as evaporites through evaporation of solutions leached from basaltic minerals in the presence of dissolved carbonate ions (simulates CO<sub>2</sub>-rich environment) and without carbonate addition (simulates CO<sub>2</sub>-poor environment), and (2) to determine what sulfate-carbonate mineral assemblages could have formed on early Mars.

#### Methods:

**Basaltic Glass.** Basaltic glass from Stapafell Mountain, Iceland was used in this study. Stapafell basalt has been previously used as a Mars analog basaltic glass [5]. Prior to evaporation experiments, basaltic glass was ground using a pulverizer with an agate mortar and pestle in ethanol for 30 minutes with a downforce of 15 daN, and then sieved to > 45 μm [6].

**Evaporation Solutions.** To create the leached solution, 1g of Stapafell was reacted with 60g of 10, 20, or 30mM sulfuric acid in 125mL Teflon lined Parr acid digestion vessels for two days at 200°C. After the two day reaction, the reactors were opened and the leached solution was separated from the remaining solid Stapafell basaltic glass and passed through a 0.2μm syringe filter.

Three sets of experiments were performed with 40mL of each of the leached solutions. In the first set, no carbonate was added. In the second set, an aliquot of ammonium bicarbonate (NH<sub>4</sub>HCO<sub>3</sub>) was added to obtain a concentration of 34mM NH<sub>4</sub>HCO<sub>3</sub>. The selected concentration of 34mM NH<sub>4</sub>HCO<sub>3</sub> corresponds to equilibrium with 1 atm of CO<sub>2</sub> at pH 2. In the third

set of experiments, the pH was increased to a specific value using ammonium hydroxide (NH<sub>4</sub>OH).

After the additions, the solution was split in half, the first portion was poured onto a watch glass in a 50°C oven and the second portion was poured onto a watch glass in a N<sub>2</sub> glovebox at room temperature. Both were then let alone and allowed to evaporate. Samples completely evaporated in 24 hours in the oven and 48 hours in the glovebox.

**Ion Chromatography (IC).** Prior to evaporation, the solution was analyzed for sulfate and carbonate by ion chromatography using an Integrion instrument equipped with AS-11 column with a 20 μm injection volume. A sample aliquot was diluted with MilliQ water with a dilution factor of 26 and 12 for sulfate and carbonate analysis, respectively.

**Inductively Coupled Plasma Optical Emission Spectroscopy (ICP-OES).** A portion of solution leached by H<sub>2</sub>SO<sub>4</sub> from Stapafell basaltic glass was analyzed by the Avio 220 Max to determine the concentration of silicon, magnesium, calcium, sodium, and potassium. For each solution 1:10 and 1:50 dilutions were prepared due to the high concentration of magnesium and low concentration of potassium in the solutions.

**X-Ray Diffraction (XRD).** The evaporites were analyzed using the PANalytical X'Pert Pro instrument equipped with Co Kα radiation at 45 kV and 40 mA, 0.02°2θ step size, and 1-min counting rate. Samples were placed on a zero background slide and scanned from 4-80°.

**Evolved Gas Analysis (EGA).** Evaporite samples were analyzed using a Labsys Evo Simultaneous Thermal Analysis instrument (Setaram Instrumentation, KEP technologies) connected to a quadrupole mass spectrometer (Thermostar GSD 320, Pfeiffer Vacuum Incorporated). The technique was applied to confirm the presence of carbonates and sulfates.

**Evaporation modeling.** The evaporation reactions were modeled using Geochemist's Workbench's React function to determine which minerals should be thermodynamically stable based on initial concentrations measured by ICP-OES and IC.

#### Results:

**Table 1.** Phases identified from each experiment.

Exp #	H <sub>2</sub> SO <sub>4</sub> (mM)	NH <sub>4</sub> HCO <sub>3</sub> (mM)	pH*	Phases identified by XRD	
				H <sub>2</sub> SO <sub>4</sub>	
7	10	0	4.05	gypsum, anhydrite, hexahydrate	

1	20	0	2.09	gypsum, hexahydrate, pentahydrate	anhydrite, pentahydrate
2	30	0	1.8	gypsum, hexahydrate, pentahydrate	anhydrite, pentahydrate
<b>H<sub>2</sub>SO<sub>4</sub> + NH<sub>4</sub>HCO<sub>3</sub></b>					
8a	10	34	8.27	gypsum, hexahydrate	anhydrite, hexahydrate
3	20	34	6.95**	gypsum, boussingaultite, hexahydrate	boussingaultite, hexahydrate
5	20	34	6.95	gypsum, boussingaultite, hexahydrate	boussingaultite, hexahydrate
4	30	34	6.38**	gypsum, boussingaultite, hexahydrate	boussingaultite, hexahydrate
6	30	34	6.38	gypsum, boussingaultite, hexahydrate	boussingaultite, hexahydrate
<b>H<sub>2</sub>SO<sub>4</sub> + NH<sub>4</sub>HCO<sub>3</sub> + NH<sub>4</sub>OH</b>					
8b	10	34	10	gypsum, boussingaultite, hexahydrate	anhydrite, hexahydrate
9a	20	34	10	gypsum, boussingaultite, hexahydrate	bassanite, boussingaultite, hexahydrate
9b	20	34	11	gypsum, boussingaultite, hexahydrate	bassanite, boussingaultite, hexahydrate

\*pH before the evaporation started, \*\*pH assumed to be equivalent to Exp 5 and 6 but was not taken before evaporation.

X-ray diffraction analysis revealed that the evaporite samples formed from 20mM and 30mM H<sub>2</sub>SO<sub>4</sub> leached solutions with no carbonate addition contained hexahydrate (MgSO<sub>4</sub>·6H<sub>2</sub>O), pentahydrate (MgSO<sub>4</sub>·5H<sub>2</sub>O), gypsum (CaSO<sub>4</sub>·2H<sub>2</sub>O), anhydrite (CaSO<sub>4</sub>), and potentially thenardite (Na<sub>2</sub>SO<sub>4</sub>) (Table 1). The evaporite formed from 10 mM H<sub>2</sub>SO<sub>4</sub> leached solution contained hexahydrate, gypsum, anhydrite, and potentially thenardite.

In the experiments where 34mM ammonium bicarbonate was added in pH adjusted and unadjusted solutions, boussingaultite ((NH<sub>4</sub>)<sub>2</sub>Mg(SO<sub>4</sub>)<sub>2</sub>·6H<sub>2</sub>O), an ammonium magnesium sulfate formed along with hexahydrate and gypsum (Table 1). No crystalline carbonates were detected. This was unexpected since thermodynamic modeling results supported the formation of magnesium and calcium carbonate (Fig. 1) as opposed to the magnesium and calcium sulfates identified in the experiments.

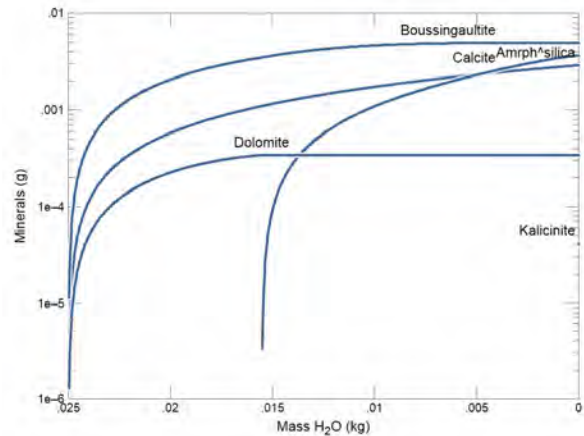


**Figure 1.** Thermodynamic modeling of minerals formed through evaporation of solution with composition from Evaporation experiment 5 performed in N<sub>2</sub>-purged glovebox at room temperature.

When comparing actual evaporites with modeling on Geochemist's Workbench, boussingaultite forms along with calcite or dolomite and sometimes a sodium sulfate. As seen in Fig 1, the modeling predicted the formation of boussingaultite, amorphous silica, calcite, dolomite, and kalcinite for experiment 5. While amorphous silica is not detectable with the XRD, the modeling does predict carbonates which have not been found in any of our evaporites.

Although crystalline carbonates were not detected, data from the EGA analysis showed a small release of CO<sub>2</sub> which could correspond to amorphous calcium carbonate. In addition, it also showed the release of some SO<sub>2</sub> in support of detection of sulfate minerals with XRD.

**Discussion:** Based on the results from the experiments, crystalline sulfates formed with and without carbonate addition, but crystalline carbonates were not detected. The XRD data identified that hexahydrate and gypsum formed at all concentrations of H<sub>2</sub>SO<sub>4</sub> and with and without carbonate present. Anhydrite formed without carbonate present or with carbonate in the solutions leached with 10 mM H<sub>2</sub>SO<sub>4</sub>. It was also found that sulfate precipitation was not sensitive to the initial concentration of H<sub>2</sub>SO<sub>4</sub> as almost the same minerals form at all three concentrations. Using NH<sub>4</sub>HCO<sub>3</sub> as a carbonate source ended up effecting the solution more than was anticipated. The ammonium remained stable in solution instead of volatilizing as ammonia gas because of solution buffering by a mixture of NH<sub>4</sub>HCO<sub>3</sub> and NH<sub>4</sub>OH. As a result, boussingaultite formed in all samples treated with NH<sub>4</sub>HCO<sub>3</sub>.

The most interesting thing found in the experiments was that no crystalline carbonates were detected by the XRD. The results indicate that dissolved carbonates do not affect solution speciation and sulfates were the

dominating minerals despite the presence of variable concentrations of carbonate. This was not expected as both modeling and terrestrial observations support the formation of crystalline carbonate [7]. One possible reason for this is if any crystalline carbonates formed, they were quickly dissolved back into the solution before the evaporation was completed and then precipitated as amorphous carbonate. Alternatively, the precipitation reaction was fast leading to formation of only amorphous carbonates. Formation of amorphous calcium carbonate was supported by detection of evolved CO<sub>2</sub>, however, its formation pathway could not be constrained.

Our results suggest that evaporation of aquatic systems containing dissolved sulfate and carbonate on Mars would mainly lead to precipitation of various sulfate minerals of Ca and Mg. Crystalline carbonate would likely not form, however, an amorphous carbonate can be expected to form. The lack of instrumentation to identify amorphous carbonate on Mars could result in an underestimation of carbonate on the planet.


**Conclusions:** Formation of Ca and Mg sulfates (hexahydrate, gypsum, and anhydrite) was observed in the solutions leached from Mars analog basaltic glass by 10, 20 and 30mM H<sub>2</sub>SO<sub>4</sub> with and without the presence of dissolved carbonate. The only carbonate formed was amorphous calcium carbonate. As a next step, sodium bicarbonate (NaHCO<sub>3</sub>) will be used as the carbonate source to eliminate the creation of bous-singaultite and NaOH will be used to adjust pH. In addition, the synthesized evaporites will be reexamined with XRD to see if the mineralogy changes over time.

**References:** [1] Bonello G. et al. (2005) *LPS XXXVI*, Abstract #1996. [2] Clark B. C. et al. (2005) *Earth Planet. Sci. Lett.*, 240(1), 73-94. [3] Lane M. D. (2005) *LPS XXXVI*, Abstract #2180. [4] Squyres S. W. et al. (2004) *Science*, 306, 1709-1714. [5] Viennet J. - C., Bultel B. and Werner S. C. (2019) *Chem. Geol.*, 82-95. [6] Ralston S. J. et al. (2023) *Earth Planet. Sci. Lett.*, 603, 117987. [7] Tosca N. J. and Tutolo B. M. (2023) *Elements*, 19(1), 15-21.



# LPI Intern Directory


Summer 2023



**Elana Alevy**

● INTERN TYPE  
LPI Intern


● ADVISOR  
Nicole Nevill



**Amelia Ascione**

● INTERN TYPE  
LPI Intern


● ADVISOR  
Rachel Slank



**Victoria Burnette**

● INTERN TYPE  
LPI Intern


● ADVISOR  
Prajka Mane



**Candice De Anda**

● INTERN TYPE  
LPI Intern


● ADVISOR  
Elizabeth (Liz) Rampe



**Andrew Gmerek**

● INTERN TYPE  
LPI Intern


● ADVISOR  
Matt Weller



**Danielle Kallenborn**

● INTERN TYPE  
LPI Intern


● ADVISOR  
David Kring



**Chloe Locke**

● INTERN TYPE  
LPI Intern


● ADVISOR  
Thomas Barrett



**Kyla Malo**

● INTERN TYPE  
LPI Intern


● ADVISOR  
Kennda Lynch



**Jared McCallion**

● INTERN TYPE  
LPI Intern


● ADVISOR  
Samuel Lawrence



**Pragya Raghav**

● INTERN TYPE  
LPI Intern


● ADVISOR  
German Martinez



**Mia Rudin**

● INTERN TYPE  
LPI Intern


● ADVISOR  
J. Brian Baha



**Alexa Schultz**

● INTERN TYPE  
LPI Intern

● ADVISOR  
Patrick McGovern



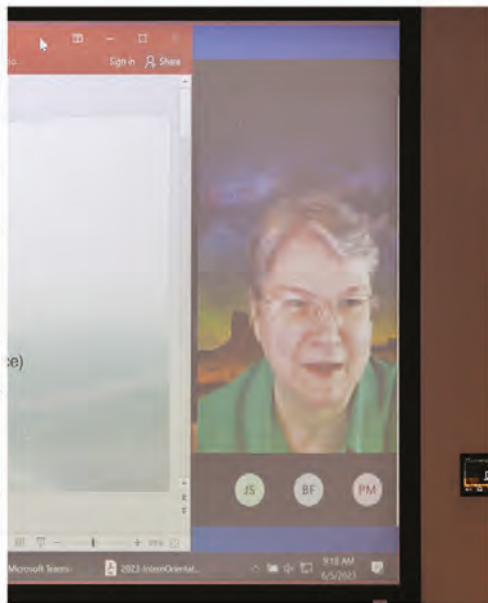
**Madeline Walters**

● INTERN TYPE  
LPI Intern

● ADVISOR  
Tanya Peretyazhko





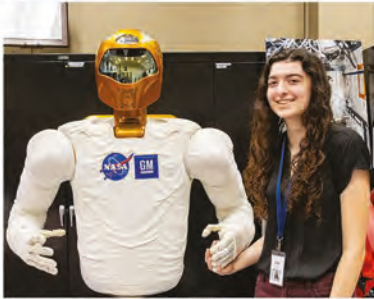


## LPI Summer Intern in Planetary Science Orientations - June 5, 2023



# LPI Summer Intern and staff barbeque June 15, 2023





The Robotic Systems Technology Branch is responsible for the research, engineering, development, integration, and application of robotic hardware and software technologies for specific flight and ground robotic system applications in support of human spaceflight.

June 29, 2023





Lunar Curation - The Johnson Space Center facility consists of storage vaults for lunar samples, laboratories for sample preparation and study, and a vault for sample data and records. Nearly 400 lunar samples are distributed each year for research and teaching projects.

The Experimental Impact Laboratory (EIL) is home to three distinct accelerators, each of which is used to model the effects of impact and shock on planetary surfaces and materials in its own unique way. Near-vacuum conditions (pressures much below 1 torr) are typical for impacts in the EIL.

Everett Gibson was showing the Apollo tools and Core Tube. Samples of: Hand Sample Meteorites: Iron Meteorite/ Allende Carbonaceous Chondrite Meteorite/ ALH76001 Ordinary Chondrite Meteorite.

July 6, 2023



# Midterms July 12, 2023

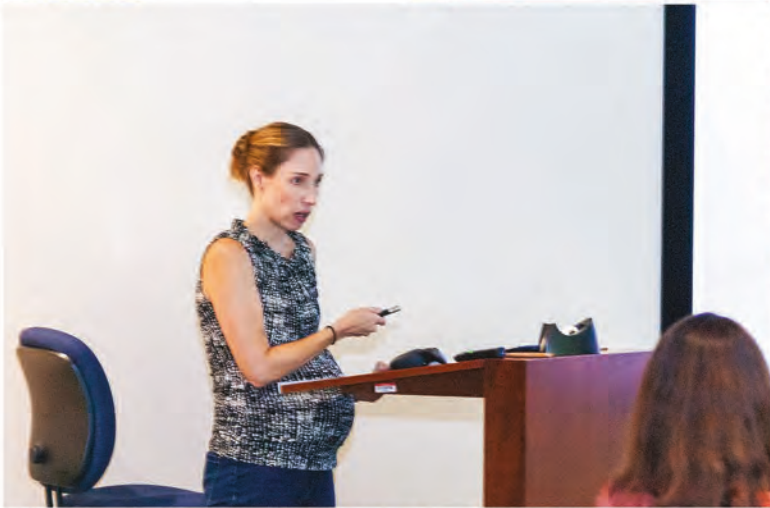




Near the Johnson Space Center in Houston, Texas, at the Sonny Carter Training Facility, NASA operates the Neutral Buoyancy Laboratory (NBL), a facility for astronaut training with a neutral buoyancy pool.[2] The centerpiece of the NBL is a large indoor swimming pool,[3] where astronauts may practice for prospective missions by simulating EVA activities. In order to replicate the microgravity that astronauts experience during spaceflight, trainees wear suits that offer neutral buoyancy.

July 14, 2023





Throughout the summer, the interns attended Planetary Science and Professional Development Seminars, where they were exposed to various fields in Planetary Science where they were provided with career growth opportunities.



